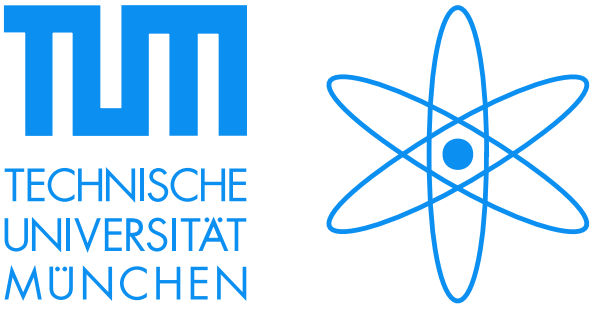

Studies of Diffractive Particle Production at COMPASS

Diploma Thesis

by

Stefanie Grabmüller

PHYSIK-DEPARTMENT E18

TECHNISCHE UNIVERSITÄT
MÜNCHEN

DEZEMBER 2005

Abstract

The COMPASS experiment at CERN investigates the structure and spectroscopy of hadrons with high intensity muon and hadron beams.

One important part of the physics program with pion beam is the detection of exotic states via diffractive dissociation. The most famous candidates for exotics are $\eta\pi^-$ systems with the forbidden quantum number $J^{PC} = 1^{-+}$.

The major part of this thesis presents an elementary analysis of the diffractive dissociation of π^- into charged particles based on data of the first hadron beam time 2004.

Double-sided silicon microstrip detectors provide excellent spatial resolution and are therefore used for beam definition and track reconstruction in the target region.

The ancillary experimental part of this thesis deals with the production procedure of the silicon detector modules used in COMPASS.

Contents

Chapter 1

Introduction

The main goal of particle physics is the better and better understanding of the elementary constituents of matter and the properties of the interactions between them. The experimental approach to this topic is fulfilled with the help of large particle accelerators which provide the large energies required. To access the diminutive elementary objects, the wavelength of the beam particles has to be in the order of magnitude of the object to be investigated. The creation and investigation of many of the constituents demand large energies as well due to their high masses. Modern accelerators and the respective experimental setups are so big, technically complex, and expensive, that they are operated by several groups of physicists, organized in collaborations, together.
This thesis was prepared in the framework of the COMPASS collaboration at CERN, that aims at investigating the structure and spectroscopy of hadrons with high statistics of high energy muon and hadron beams on various fixed targets. The multifarious COMPASS physics program and the state-of-the-art spectrometer designed to fulfill challenging specifications are introduced in chapter 2, as well as the software used for analyzing the data.
The strong interaction can be accessed via central production or diffractive dissociation of hadrons. Both of these interactions are to be investigated within the COMPASS agenda. To give some background knowledge for the analysis presented in this thesis, several remarks concerning diffractive dissociation with the pomeron as exchange particle are given in chapter 3.
An additional preparation for the implementation and understanding of the analysis can be found in chapter 4. There the theoretical concepts for accessing the spins of intermediate states of decays into three pseudo-scalar particles are reviewed.
The results of previous experiments with π^- beams on nuclear targets are very briefly presented in chapter 5.

In 2004 the first hadron beam time of the COMPASS experiment with π^- beam took place. An elementary analysis of the diffractive dissociation of the π^- into three charged particles is presented in chapter 6.
An overview of the data taken during this hadron run is given in chapter 7. Some studies focussing the data used for the presented analysis were performed.
Silicon microstrip detectors are used for beam definition and particle tracking in the target region of the experiment due to their excellent spatial resolution. In chapter 8 the basic operation principles of silicon microstrip detectors are presented, followed by an overview of the composition of a COMPASS silicon detector. Additionally, the production procedure for these silicon detectors is presented with supplementary improvements to be done for the coming production of modules.

Chapter 2

The COMPASS Experiment

The **CO**mmon **M**uon **P**roton **A**pparatus for **S**tructure and **S**pectroscopy is a high-luminosity fixed target experiment at the Super Proton Synchrotron (SPS) at CERN[1]. Evolved from two competing collaborations, CHEOPS[2] and HMC[3], it uses polarized muon beam and unpolarized hadron beams in basically the same spectrometer to address several physics topics concerning structure and spectroscopy of hadrons.
The proposal for the COMPASS experiment [COM96] was approved by CERN in 1996. The spectrometer was commissioned in 2001. In 2002, 2003 and 2004 physics data were taken with a 160 GeV muon beam, and in autumn 2004 also a first hadron beam time with a 190 GeV π^- beam was realized. After a technical break in 2005, the experiment will continue with an upgraded spectrometer for muon as well as hadron program from 2006 on.
An overview of the two different physics programs is given in section 2.1. The experimental setup is presented in section 2.2, focussing the setup of the first hadron beam time. Additionally the software tools used for reconstructing and analyzing COMPASS data are presented in section 2.3.

[1] **C**onseil **E**uropéenne pour la **R**echerche **N**ucléaire (European Organisation for Nuclear Research), founded in Geneva, Switzerland, in 1954. Nowadays CERN is the world's largest particle physics center. CERN is run by 20 european member states, and also many non-european states participate. For more information see [CER].

[2] **CH**arm **E**xperiment with **O**mni **P**urpose **S**etup

[3] **H**adron **M**uon **C**ollaboration

2.1 The COMPASS Physics Program

2.1.1 Physics with Muon Beam

The main goal of the COMPASS muon program is the investigation of the spin-dependent structure of the nucleon. This is arranged by the combination of polarized muon beam and polarized ^{6}LiD and NH_3 targets, respectively, where the two target materials are needed to separate the helicity distributions of the different quark flavours.
The nucleon spin is well-established to be $\frac{1}{2}$. For a long time this was supposed to be the sum of the spins of the three valence quarks, until the EMC[4] experiment obtained a contribution of quarks to the total spin of only $\approx$30%. The residual spin is now frequently assigned to polarized virtual gluons in the nucleon, while a competing explanation is given by negatively polarized strange sea-quarks in the nucleon.
After three years of data taking (2002-2004), several results for topics of interest have been published already.

Gluon Polarization $\Delta G/G$**:** Photon-Gluon Fusion (PGF) provides the most direct access to the gluon polarization $\Delta G/G$. A virtual photon emitted by the incident muon interacts with a gluon via an intermediate quark line. With this process, longitudinal spin asymmetry of open charm leptoproduction is studied via reconstruction of neutral D mesons, which emerge from the hadronization of intermediate charm quarks, from their hadronic decay products. Another approach is given by high p_T pair or high p_T single events, where any intermediate quarks hadronizing into jets with high transverse momentum are considered.
Recently the following value of $\Delta G/G$ from quasi-real photoproduction of high-p_T pairs has been published [COM05b]

$$\frac{\Delta G}{G} = 0.024 \pm 0.089(\text{stat}) \pm 0.057(\text{syst}) \tag{2.1}$$

Lambda and Anti-Lambda Polarization: The polarization of strange quarks and/or antiquarks can be measured via the longitudinal polarization of Λ and $\bar{\Lambda}$ baryons. The contribution of the strange sea quarks to the nucleon spin can be accessed by measuring the polarization of Λs from the target fragmentation. Reactions where quarks are oriented anti-parallel to the virtual photon's helicity can be selected by using a polarized muon beam with an unpolarized target.

[4] **E**uropean **M**uon **C**ollaboration

Longitudinal Spin Distribution Functions: Semi-inclusive measurement of deep inelastic scattering (DIS) of polarized leptons on proton and deuteron targets can help to decompose the nucleon spin into the valence and the sea components and determine the spin distribution functions of the different flavours for the valence and sea quarks. At COMPASS, these asymmetry measurements are performed with a longitudinally polarized target.
Results of the measurement of the longitudinal spin asymmetry A_1^d and the spin-dependent structure function g_1^d of the deuteron in the range $1\,\mathrm{GeV}^2 < Q^2 < 100\,\mathrm{GeV}^2$ can be found in [COM05c].

Transverse Spin Distribution Functions: The probability for the quark spin in a transversely polarized nucleon to be oriented parallel or antiparallel to the nucleon spin can be measured in deep inelastic scattering of longitudinally polarized muons off a transversely polarized target.
First measurements of the Collins and Sivers asymmetries of charged hadrons produced in deep inelastic scattering showed that the Collins asymmetry, as well as the Sivers asymmetry within the statistical errors, turn out to be compatible with zero [COM05a].

Transverse Λ^0 Polarization: If a Λ hyperon is produced in an unpolarized inclusive reaction and if the interaction in the production process is parity conserving, the hyperon is possibly polarized perpendicular to the production plane. The measurement of the transverse polarization of Λ^0 generated from quasi-real photo-production was not included in the original proposal, but is investigated for example by [Wie04, Gru06].

Generalized Parton Distributions (GPD): Unifying the concepts of parton distributions and hadronic form factors, generalized parton distributions provide new information about how hadrons are composed of quarks and gluons. They can be accessed in exclusive processes such as Hard Exclusive Meson Production (HEMP) and Deeply Virtual Compton Scattering (DVCS). The first of these can be investigated via ρ^0 production with the existing spectrometer, while the second one demands several upgrades for the target, a recoil detector, and the calorimeters [dHo04]. This topic was added to the COMPASS muon program only after the beginning of physics data taking.

Pentaquarks: Another item not included in the initial proposal, but added to the agenda to review results of competing experiments as NA49, is the search for new hadronic systems with a flavour content different from the usual baryonic qqq and $\bar{q}\bar{q}\bar{q}$ or the mesonic $q\bar{q}$ structures. Pentaquarks with a quark content $qqqq\bar{q}$ as Θ^+ at about 1540 MeV and the $\Phi(1860)$ have been reported. COMPASS has collected a large sample of doubly

strange Ξ^- baryons in the final state from quasi-real photoproduction and searched for the doubly strange pentaquark system, decaying according to $\Phi(1860)^{--} \rightarrow \Xi^-\pi^- \rightarrow \Lambda\pi^-\pi^- \rightarrow p\pi^-\pi^-\pi^-$, but could not confirm its existence [COM05d].

2.1.2 Physics with Hadron Beam

The COMPASS hadron program consists of three main issues. Hadronic structures of unstable particles are investigated using Primakoff reactions, spectroscopy of light quark systems and glueballs is aspired, and charmed hadrons are studied. All these three topics profit especially from the high statistics which can be taken with the COMPASS spectrometer. Pion, kaon and proton beams with momenta of few hundred GeV are foreseen here.

Primakoff Scattering: Nowadays, the nature of particles and nuclei is commonly traced back to spontaneously broken chiral symmetry, so that the predictions of the QCD[5] chiral Lagrangian are to be checked experimentally. Notably predictions of measurable quantities such as pion and kaon polarizabilites and chiral axial anomaly amplitudes can be derived from chiral perturbation theory. The γ-π and γ-K interaction, respectively, are used for the experimental investigation of these topics. It is impossible to carry out experiments on a pion or kaon target, so suchlike beam particles are scattered off a virtual photon in the Coulomb field of a high-Z nucleus. The Primakoff reaction mechanism, which is Compton scattering with virtual photons in inverse kinematics, is analyzed starting from the detection of a final photon and the scattered hadron in coincidence.

Exotic States: Strongly interacting systems other than mesons ($q\bar{q}$) and baryons (qqq) are called exotic. The only assured regulation by QCD is colour neutralization, so that bound states with more than three valence quarks or valence gluons are predicted and have to be confirmed experimentally. This is aimed at by central production as well as diffractive scattering (section 3) of pions and kaons by nuclei.
Mixtures of valence quarks and valence gluons are called hybrids. As they are merged by quarks and gluons, thus fermions and bosons, they can adopt quantum numbers forbidden for conventional hadrons. Thereby discrimination between those and exotics can be confirmed.

[5] **Q**uantum **C**hromo **D**ynamics is the gauge field theory of the strong interaction of quarks, with gluons as exchange vector bosons and colour charge of quarks and gluons. QCD is a part of the standard model.

Glueballs are constituted only of gluons. They are predicted to be flavour blind and to decay preferentially into states containing large glue components or large SU(3) singlet components like the η' or the η.
The most famous candidate for an exotic, $\eta\pi^-$ systems with the forbidden quantum numbers $J^{PC} = 1^{-+}$, are looked for with diffractive scattering.

Charmed Hadrons: Semi-leptonic decays, lifetimes and non-leptonic decays of charmed hadrons are studied. The groundstates of single-charmed baryons are observed, but still little is known about the properties of these objects. Even more unfamiliar are double-charmed baryons, which should be similar to heavy mesons, where one light quark is coupled to one heavy partner. Also charm exotics are predicted: Special interest is attended to strange-anticharmed pentaquarks ($uud\bar{c}s$ or $udd\bar{c}s$) which are expected to be either narrow resonances, or even stable against strong and electroweak decay. The same is presumed for a doubly charmed tetraquark.

2.2 The COMPASS Spectrometer

The COMPASS experiment is located at the M2 beam line (section 2.2.1) of the SPS which can provide the required high-intensity muon and hadron beams. For the different physics topics, various targets are used (see section 2.2.2). The experimental setup consists of a modern, high rate forward spectrometer with two independent magnetic spectrometer stages each featuring detectors for tracking, particle identification and calorimetry, which are briefly described in section 2.2.3. The triggers initializing the readout of the various detectors are presented in section 2.2.4. For more details of the spectrometer see [COM06].

2.2.1 The M2 Beam Line

The M2 beam line can deliver either high-intensity tertiary muon beams up to 190 GeV/c or high-intensity secondary hadron beams up to 280 GeV/c momentum to the COMPASS experiment.
The SPS accelerates protons up to momenta of 400 GeV/c. The nominal proton flux is $1.2 \cdot 10^{13}$ protons per SPS cycle[6] to the COMPASS production target T6, which consists of beryllium and whose length determines the intensity of the produced secondary beam.
The secondary pions, kaons and protons can be guided directly to the experiment,

[6] A SPS cycle lasts 16.8 seconds, during the first 4.8 seconds protons are extracted.

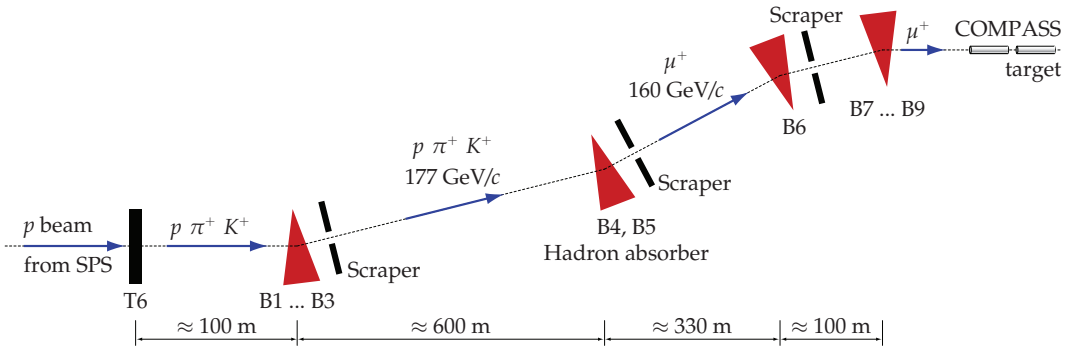

Figure 2.1: The M2 beam line for the muon program (from [Gru06])

whereby the desired momentum of beam particles can be selected with magnets and collimators. The mixture of pions, kaons and protons in the beam depends on the selected momentum. The maximum allowed hadron flux is 10^8 per SPS cycle. The typical spot size at the COMPASS target is in the order of $\sigma = 3\,\text{mm} \times 3\,\text{mm}$. Tertiary muon beam can be obtained from the decay of pions in the 600 m long beam tunnel. Due to parity violation of the pion decay the muons are polarized. With an additional hadron absorber of about 10 m beryllium the muon beam is cleaned from the remaining hadrons. The intensity of muon beam is up to $2 \cdot 10^8$ per SPS cycle, and the beam is focused to $\sigma = 10\,\text{mm} \times 8\,\text{mm}$ at the target with 16 % halo within 50 mm from the beam axis. The beam line in the muon configuration is pictured in figure 2.1.

2.2.2 The Targets

The multifaceted COMPASS physics program requires different targets additional to the different beams.

Muon target: For the muon program a polarized ^{6}LiD target, divided into two 60 cm long cells with 3 cm diameter and 10 cm separation, is used. The two cells are polarized in opposite direction by dynamic nuclear polarization with two separated microwave systems and cooled down to $\approx$ 100 mK by a dilution refrigerator. The cells are situated in a superconducting solenoid magnet with 2.5 T in beam direction. Additionally a dipole coil can produce a transverse field up to 0.5 T. For the 2007 muon beam time the target will be redesigned with three cells (30 cm, 60 cm and 30 cm long) to reduce systematic effects.

Hadron targets: In the hadron program various target materials are used according to the different demands of the investigated processes. Primakoff measurements require target materials with high atomic numbers and therefore high radiation lengths, to improve the ratio between the Coulomb and the diffractive cross section in the region of the momentum transfer $|t| \leq 10^{-3}(\mathrm{GeV}/c)^2$. The study of diffractively produced mesons conversely needs targets with low atomic number in order to minimize multiple scattering in the target material.
During the hadron beam time 2004 these two programs had to be performed in parallel, so that lead, copper and carbon targets in the form of cylinders with 3 cm diameter were used (for a detailed itemization see section 7.1).
Both measurements are characterized by small momentum transfer to the target nuclei, so that hard scattering events have to be rejected. The recoil energy of the target nucleus (or its fragments) is measured with a barrel-shaped veto system, called Veto Box, which surrounds the target. The Veto Box consists of 12 scintillator plates and 96 lead glass blocks in a cylindrical symmetry. The recoil energy can be reconstructed using the energy loss in the scintillator in combination with the Cherenkov light produced in the lead glass.
For future studies of exotic hadrons from diffractive processes and central production a liquid hydrogen target will be used.

2.2.3 The Detectors

The COMPASS spectrometer consists of the target region and two stages designed for detecting particles with small and large momenta, respectively. The first stage is the large angle spectrometer (LAS) starting with the first bending magnet *SM1* with a bending power of 1.0 Tm, and the second bending mangnet *SM2* with a field of strength 5.2 Tm marks the beginning of the small angle spectrometer (SAS). The absorbing detectors in the large angle spectrometer (calorimeters and muon filter) have a central hole which covers the acceptance of the small angle spectrometer, which provides a much better resolution for particles with high momentum due to the stronger magnet and the longer ranges it spans.
The present tracking detectors, detectors for particle identification and calorimeters are presented here. A schematic overview of the spectrometer used during the hadron beam time 2004 is shown in figure 2.2.

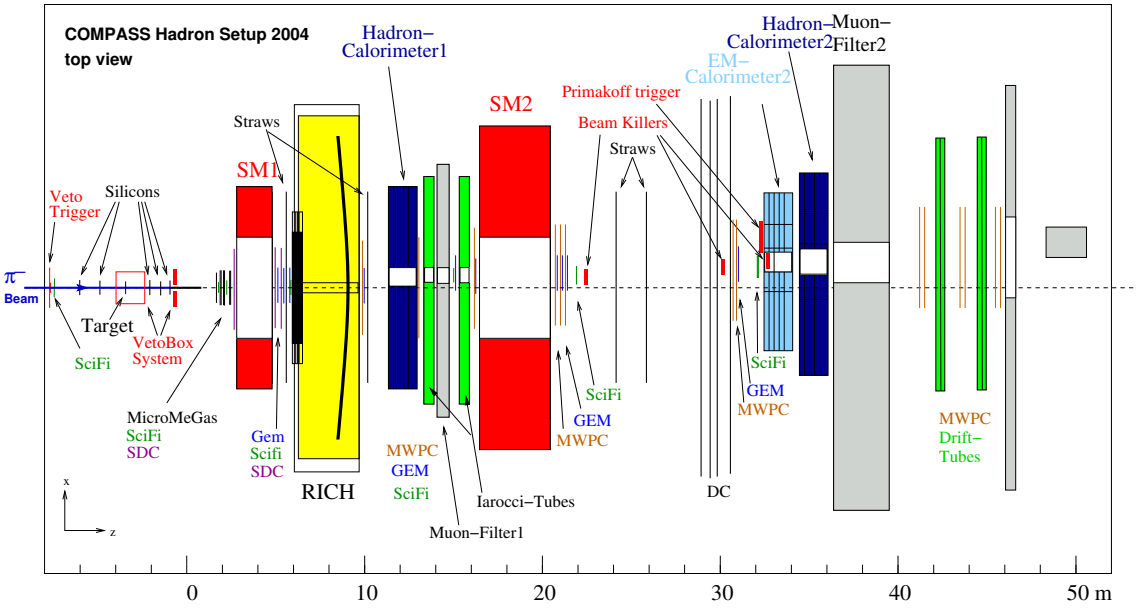

Figure 2.2: COMPASS spectrometer of the first hadron beam time 2004

2.2.3.1 Tracking Detectors

The tracking detectors are distributed over the whole length of the spectrometer and assembled in so-called *stations*. The Very Small Area Trackers (VSATs) cover the beam region up to a radial distance of 2.5-3 cm, they are designed to stand the high particle rates of the beam. The Small Area Trackers (SATs) are micropattern gas detectors which cover the radial region from 2.5 cm to 30-40 cm. The outermost region with the lowest particle flux is covered by Large Area Trackers (LATs) as multi-wire proportional chambers and drift chambers.

Very Small Area Trackers: The VSATs are the only trackers which stand the full rate of the beam and do not have blind spots in their respective centers.
The **Beam Momentum Station** (BMS) is placed around the dipole magnet which makes the muon beam roughly horizontal, located about 100 m upstream of the target. It consists of four scintillator hodoscopes and two scintillating fiber hodoscopes of whose hits the bending radius in the magnetic field and therefrom the momentum of the beam particle can be determined. During the hadron beam time the BMS was removed due to the high hadronic interaction length of its detectors.
The **Scintillating Fibers** (SciFis) provide an excellent time resolution of $\approx$ 400 ps and a spatial resolution of $\geq$ 130 μm, so they are used particularly for timing information. During muon data taking, two SciFis are part of the beam telescope upstream of the target, and six SciFis are distributed

in the rest of the spectrometer. During hadron data taking, some of them were removed due to their high interaction length.
The **Silicon Microstrip Detectors** complement one another with the SciFis perfectly for beam definition, as they provide a spatial resolution of $5 - 14\,\mu$m depending on the cluster size, while the time resolution is $1.5 - 3$ ns. For muon data taking, three stations are part of the beam telescope, while during hadron beam time only two stations are implemented there and three further stations are located downstream of the target to perform accurate vertex and track reconstruction.

Small Area Trackers: The **MicroMeGas** (Micro Mesh Gas detectors) and **GEM**s (Gas Electron Multipliers) use very small gas volumes with different types of gas amplification to obtain good spatial and time resolution. Three MicroMeGas with an active area of 40 cm $\times$ 40 cm, a spatial resolution of about 70 μm, and a time resolution of about 10 ns are located immediate in front of *SM1*. More downstream in the spectrometer, 11 GEMs with an active area of 32 cm $\times$ 32 cm, a spatial resolution of about 50 μm, and a time resolution of 12 ns are distributed. Both of these detector types have dead and insensitive, respectively, zones with 5 cm diameter in the center.

Large Area Trackers: To cover larger areas, gas detectors with anode wires of different types are used. **Multi Wire Proportional Chambers** (MWPC) can only determine which wire had a signal, while with **Drift Chambers** (DC), **Straw Drift Chambers** (Straws) and the **W45** the drift time is used to improve the spatial resolution. These detectors cover areas from 1.2 m $\times$ 1.2 m (DC) up to 5.2 m $\times$ 2.6 m (W45), with spatial resolutions between about 200 μm and 2 mm. Their dead zones differ from 20 cm to 1 m diameter, dependent on the typ of chamber and the position downstream. The dead zones of straws, DCs and MWPCs are covered by GEMs which are directly mounted to them (cf. figure 2.2).

2.2.3.2 Particle Identification

COMPASS uses several systems to identify particles:

RICH: The **R**ing **I**maging **CH**erenkov counter in the first spectrometer stage is based on the appearance of a cone of Cherenkov light if a particle crosses a medium faster than light. Via the opening angle θ of this cone the velocity of the particle can be determined, and, combined with the momentum, its mass can be derived. The COMPASS RICH is filled with C_4F_{10} gas during the muon program. This allows to separate pions, kaons and protons in the

occuring energy region. For hadron data taking, C_4F_{10} is unsuitable, so the RICH is filled with nitrogen and switched off.

CEDARs: The principle of the **CE**renkov **D**ifferential counters with **A**chromatic **R**ings is similar to the one of the RICH. During hadron program, two CEDARs were mounted in the beam line to tag pions and kaons, but they did not work properly.

Muon Filters: At the end of each spectrometer stage a muon filter is installed. They consist of tracking detectors before and behind a massive absorber (60 cm iron for MF1 and 2.4 m concrete for MF2, respectively). Muons are the only particles having a penetration power sufficient to traverse these absorbers, so every particle detected to have crossed the absorbers can be assumed to be a muon.

2.2.3.3 Calorimetry

The energies of electromagnetic and of hadronic interacting particles are measured with the two types of calorimeters:

HCALs: At the end of each spectrometer stage, immediately before the muon filters, **H**adronic **CAL**orimeters are installed. They consist of scintiallator slices sandwiched between plates of iron and steel, respectively. Scintillating light created by hadronic interaction is collected in wavelength shifters and detected by photo multipliers. Out of this, the energy of a hadronic interacting particle can be determined. Electromagnetic interactions are excluded in the HCALs by shielding with an electromagnetic calorimeter (ECAL2) and a lead wall equivalent to 18 radiation lengths, respectively, in front of HCAL2 and HCAL1.

ECALs: The **E**lectromagnetic **CAL**orimeter ECAL2 consists of segmented lead glass blocks and is mounted right in front of the HCAL2[7]. Electrons and photons are absorbed and produce scintillation light which can be detected by photo multipliers. Hadrons are supposed to loose only a small part of their energy by electromagnetic interaction and so to cross the ECAL and deposite their energy in the subsequent HCAL.

[7]The ECAL1 supposed to be mounted in front of HCAL1 was not fully equipped for the beam time 2004, but is planned to be operationable from 2006 on

2.2.4 The Triggers

If some thresholds in detectors and calorimeters are exceeded, this causes a trigger signal which induces the readout of all detectors at a certain time particularly dependent on the latency due to the time of flight of the particles. This defines an *event*. The muon and the hadron program feature two completely different sets of triggers.

Muon Triggers: The various muon triggers are to select PGF or DIS processes with several trigger hodoscopes, see for example [Nag05] for information.

Hadron Triggers: The hadron triggers have several elements in common:
Beam definition is provided by requiring coincident hits in two scintillator counters centered in the beam trajectory. It is completed by a veto system upstream the Veto Box with a central hole with $\sim 4\,\text{cm}$ diameter to discard beam particles which did not pass the target.
The large-angle veto downstream of the Veto Box rejects events with particles falling outside the acceptance of the calorimeters due to emission at large angles.
The dedicated physics triggers are described in the following:
The **Prim_1** trigger is activated by a hit in the Primakoff Hodoscope which detects scattered pions in the momentum range 20-110 GeV/c. The photon has to deposite an energy of at least 40 GeV in the ECAL2.
The **Prim_2** trigger selects Primakoff events with scattered beam particles holding less than 20 GeV and therefore not hitting the hodoscope. An energy deposit of 100 GeV in ECAL2 is required instead.
The **Diff_1** trigger responds to the decay $\eta \rightarrow \pi^+\pi^-\pi^0$ by requiring hits of two or more charged particles in the Multiplicity Counter, a scintillator located between the Veto Box and the downstream silicon telescope. As the energy of the produced π^0 is small, no ECAL2 threshold is required by this trigger. Additionally, a **Beam Killer** veto is introduced. It consists of three small scintillators centered in the beam trajectory and mounted between the SM2 magnet and the ECAL2. These plastic scintillator disks with a diameter of 5 cm and a thickness of 5 mm are to be hit by beam particles which are not scattered by the target.
The **Diff_2** trigger is to select the decay $\eta \rightarrow 2\gamma$ by the γ signals in ECAL2 of typically each 40 GeV and requirement of a multiplicity equal to 1. This trigger was not realized in 2004.
The **Charge Exchange** trigger is activated by zero multiplicity in the Multiplicity Counter and an additional ECAL2 threshold of 40 GeV.
The **Central Production** trigger is still being optimized for being used in the future.

2.3 The COMPASS Reconstruction and Analysis Software Tools

Modern high energy physics experiments analyze their data with software tools customly developed to fit the requirements of high energy physics or even specific demands of the experiment itself. In this section the software tools which were used to perform the preparatory work and the analysis presented in chapter 6 are briefly introduced.

2.3.1 The ROOT Framework

The basic software environment for the analysis of COMPASS data is an object oriented framework written in C++ and developed at CERN, called ROOT [Bru97, ROO]. It provides basic utilities and services useful for analyzing high energy physics data. Procedures for input and output are optimized for the high amount of data. The storage of data is organized in so-called *trees* on an event-by-event basis. The data are structured in *branches*. Data in a tree can be selected by cuts on various parameters.
Histograms for storing, displaying and analyzing up to three parameters at one time and fitting routines based on the Minuit package provide access to the data and can visualize them.
The tools, CORAL and PHAST, for reconstructing and analyzing data in COMPASS (see the following sections) are linked to ROOT as well.

2.3.2 Event Reconstruction with CORAL

The COMPASS raw data contains the digitalized values of all detectors in the spectrometer. These are time informations, signal amplitudes and scalar values. To permit physics analysis these informations have to be converted to particle trajectories with three-dimensional vectors of momenta and known charge of the particles. This is performed by CORAL, the **CO**MPASS **R**econstruction and **A**na**L**ysis project [COR] which is developed by the COMPASS collaboration and under constant improvement and optimization. CORAL processes the raw data and reconstructs tracks and vertices of each event in several steps. The output is stored in **M**ini **D**ata **S**ummary **T**ables (mDSTs) on which physics analysis can be performed by PHAST.
The first step of the reconstruction procedure is the *decoding* of the raw data.

Thereby the hardware identifiers are mapped to the logical channels of the detectors.
Then the digitized values of the logical channels are transformed to *hits* in three-dimensional space with additional time information and amplitudes. For this step accurate alignment information and calibration data for the detectors is required.
The found hits are to be combined to tracks representing particles during the three-stage *tracking* procedure. Within the *pre-pattern* step track segments are reconstructed in different regions of the spectrometer. These segments are connected to full tracks during the *bridging* procedure. In the third step the optimal track parameters and corresponding error matrices are calculated by a Kalman filter. During the whole procedure, χ^2 cuts are applied to improve the track quality.
After the track reconstruction *vertexing* is performed, that means that the interacting points of the event are ascertained.
The mDST files to be used in physics analysis are created by the PHAST module of CORAL, so that they fit the standards of the analysis software.
An overview of the whole reconstruction procedure with more details and explanations can be found in [Gru06] amongst others.

2.3.3 Physics Analysis with PHAST

The mDST files are analyzed by the object oriented **PH**ysics **A**nalysis **S**oftware **T**ool (PHAST) written in C++ [PHA]. They contain every information that is necessary for common analysis. They provide an object containing stable information like magnetic fields, material maps and detector geometric information. For each event an object exists which contains all reconstructed tracks, particles, vertices, and calorimeter values.
The analysis is performed by specific functions to be written by the user. These functions are executed for every event in the mDST files. They have full access to all reconstructed data, and can select single events and analyze them. The output can either be written into a *MicroDST* file to be processed by PHAST again for further analysis, or into a ROOT tree for final analysis, that means final selection of events and visualizing the relevant data.

Chapter 3

Diffractive Dissociation of Hadrons

Diffractive dissociation of hadrons is a convenient method of investigating the strong interaction, complementary to central production. In this scattering process the incident hadronic particle h only grazes the target nucleus A. The recoiled nucleus A' remains intact, while the particle itself is excited:

$$h + A \rightarrow X + A' \tag{3.1}$$

The generated resonance or particle X subsequently decays and may be reconstructed starting from its decay products. Via its mass spectrum and its characteristics (e.g. spin) one can study the properties of the strong interaction and search for new or even exotic hadronic states, e.g. glueballs and hybrids.
The exchange particle of process (3.1) is the *pomeron* $\mathbb{P}$, which can be pictured as a multi-gluon state. It's theoretically described by the pomeron trajectory in the framework of Regge theory, which is introduced in section 3.3.
Some general remarks on the dynamics of diffractive dissociation and an overview of theoretical ideas which are useful in analyzing experimental data are presented in section 3.1. In section 3.2 it is shown how the size of the diffracting

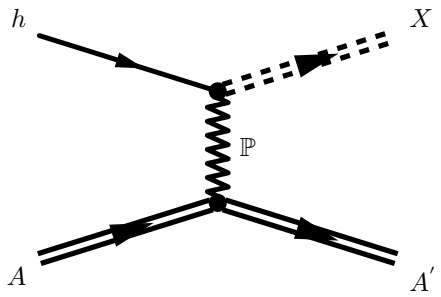

Figure 3.1: Diffractive dissociation

object can be directly derived using concepts from optics.

3.1 General Remarks

In diffractive dissociation, the target nucleus is not directly hit, but only touched by the projectile with an impact parameter which is in the order of the range of the strong interaction ($\approx 10^{-15}$ m). The squared four-momentum transfer t[1]

$$t = \mathsf{q}^2 = (\mathsf{p}_h - \mathsf{p}_X)^2 = (E_h - E_X)^2 - (\vec{p}_h - \vec{p}_X)^2 \tag{3.2}$$

(with $\mathsf{p}_{h,X}$ the four-momentum-vector, $E_{h,X}$ the energy and $\vec{p}_{h,X}$ the three-momentum-vector of particle h and X, respectively) from the projectile to the target is so small ($t \ll 1\,(\mathrm{GeV}/c^2)$), that the target has a chance to remain intact. At very small t, elastic scattering is a special case of diffractive interaction.
The energy which is transferred to the target in case of no excitation depends on the mass of its constituents and decreases with increasing mass

$$E_{trans} = \frac{|t|}{2m_A} \tag{3.3}$$

If the momentum of the incident particle h and the mass of the target nucleus m_A are high enough, the fraction of energy transferred becomes negligible, so that one can assume the energies of incident and outgoing particles, E_h and E_X, to be commensurate.
If the target nucleus A remains in ground state, there is no exchange in intrinsic quantum numbers between the incident particle and the nucleus, which means that the particles h and A have the same intrinsic quantum numbers as the particles X and A', respectively. Their spin and parity may change, but are generally expected to follow the empirical *Gribov-Morrison rule*

$$P_f = P_i(-1)^{\Delta J} \tag{3.4}$$

with P_f and P_i representing the parity of the initial and final systems and ΔJ the change of spin. So, change of parity corresponds to the net gain in spin. This corresponds to the minimum transfer of orbital angular momentum. The rule implies some selective dynamical mechanism, which means that not all energetically possible states are diffractively produced. Nevertheless, it is an empirical relation whose dynamical origin has still to be understood and is even contra-

[1] In the following $\hbar = c = 1$, so that in equations energy, mass and momentum transfer are all given in GeV. For a better discrimination between energy and momentum transfer, however, numerical data for momentum transfer are given in GeV/c.

dicted by some data.
Some theoretical concepts which are useful for analyzing data are listed below (cf. [Gou83]):

- The **Optical Theorem** relates the forward-scattering amplitude $f(s,t)$ (where s is the squared center of mass energy) to the total cross section σ_T

  $$\sigma_T = 4\pi \,\mathrm{Im} f(s,0)/k \tag{3.5}$$

  with k the wave number of the incident particle.

- **Dispersion Relations** connect the real part to the imaginary part of $f(t)$ and therefore, in combination with the optical theorem, link ρ, the ratio of the real to the imaginary part of $f(t)$, to σ_T.

- **Geometrical Scaling** assumes that, at high energies, the elastic scattering amplitude is purely imaginary and a function of the effective interaction radius R only. For spin independent interactions this assumption results in

  $$f(s,t) = i\, R^2(s)\, f[tR^2(s)] \tag{3.6}$$

  so that follows

  $$\sigma_{el} \sim \sigma_T \sim b \sim R^2(s) \tag{3.7}$$

  with b the slope parameter of the differential cross section (discussed in more detail in section 3.2).

- The hypothesis of **Factorization** of the diffractive vertex leads to scaling relations between diffractive dissociation, elastic scattering and the total cross section. Factorization requires that each scattering amplitude is proportional to the product of the coupling constants $g(t)$ at each vertex. So the ratio of diffractive dissociation to the elastic cross section is a constant independent of the target particle at given values of s, the Feynman scaling variable $x_F = p/p_{\parallel,max}$ and t

  $$\frac{\mathrm{d}^2\sigma/\mathrm{d}t\mathrm{d}x_F}{\sigma_{el}} = \left[\frac{g_{hX}(t)\cdot g_{AA}(t)}{g_{hh}(t)\cdot g_{AA}(t)}\right]^2 = C_h(s,x_F,t) \tag{3.8}$$

  The same is true for different hadrons h dissociating at the same target A only when using specific models for the diffractive amplitude. If diffractive dissociation is caused by the triple-pomeron amplitude and the total cross section by simple pomeron exchange, the ratio of diffractive dissociation to

the total cross section is independent of the dissociating hadron

$$\frac{\mathrm{d}\sigma/\mathrm{d}t\mathrm{d}x_F}{\sigma_T} = C_A(s, x_F, t) \tag{3.9}$$

Both of these rules have been tested experimentally and have been found to hold within experimental accuracy, so that (due to the second rule) the triple-pomeron representation of the diffractive amplitude is validated.

- The **Finite Mass Sum Rule** relates the high mass diffractive cross section, which is quite smooth, to the low mass one, with a prominent resonance-like structure. It is an extension to the finite energy sum rule of total cross sections and derived for triple-Regge amplitudes using analyticity and crossing symmetry. With the cross-symmetric variable $\nu = m_X^2 - m_h^2 - t$, the extrapolation of the high ν behaviour of the function $\nu(\mathrm{d}^2\sigma/\mathrm{d}t\mathrm{d}\nu)$ into the low ν region substitutes the average behaviour of the resonances (including elastic scattering).

- **Regge Theory** provides a framework which explains many features of hadronic diffractive interaction in a simple way. Based on Regge trajectories $\alpha(t)$ (see figure 3.2) and residue function $\beta(t)$, it approaches total cross sections and cross sections for elastic scattering and diffractive dissociation. This topic will be covered in more detail in section 3.3

3.2 Application of Optical Concepts to Hadronic Waves

Historically the treatment of hadronic waves was supported by the optical analogy. Hadrons can be considered as plane waves when propagating in free space and scattering with other hadrons or nuclei: The wavelength λ of the incident hadrons is much smaller than the dimensions R of the diffracting object (short wavelength condition, $kR \gg 1$ with $k = 2\pi/\lambda$) if the laboratory momentum of the incoming hadrons is in the order of GeV. The large distance condition $R/D \ll 1$ is also fulfilled, as the distance D at which the scattered hadrons are observed behind the scatterer is at least 1 cm, which means $R/D \simeq 10^{-13}$. As in all experiments up to now kR was never larger than 10^4, the relative value of these two relations, kR^2/D, is always smaller than 10^{-9}. Therefore hadron-hadron and hadron-nucleus scattering are analogous to Fraunhofer diffraction (defined by $kR^2/D \ll 1$).
The scattering amplitude $f(\vec{q})$ of a hadronic diffraction process is proportional to

the Fourier transform of the profile function $\Gamma(\vec{a})$ of the diffracting object (with $\vec{q}$ momentum transfer and $\vec{a}$ a space vector in the object starting at its center) (for details concerning this section see [AJM76]). If the profile function is spherically symmetric, as it is assumed for nuclei in this thesis, the scattering amplitude can be written as

$$f(\vec{q}) = ik \int_0^\infty \mathrm{d}a \, a\Gamma(a) J_0(qa) \tag{3.10}$$

with the Bessel function J_0.
So from the diffraction patterns of the differential cross sections one may calculate the profile functions. Experimentally it is found that the hadron-hadron differential cross section close to forward direction, i.e. at very small t, is Gaussian in the scattering angle. So the scattering amplitude is given as

$$f(q) = e^{-q^2R^2/4} \tag{3.11}$$

where R is the radius of the nucleus. If b is the slope of the logarithm of the differential cross section when plotted versus $|t| = h^2q^2$, it follows that the radius of the diffracting object is given by

$$R = h\sqrt{2}\sqrt{b} \approx 0.3\sqrt{b \ [\mathrm{GeV}^{-2}]} \text{ fm} \tag{3.12}$$

and can be directly read off the plot of the differential cross section for very small t.
A more realistic, but still quite simple, model for a nucleus leads to the profile function

$$\Gamma(a) = e^{-\frac{R^2+a^2}{4B}} I_0\left(\frac{aR}{2B}\right) \tag{3.13}$$

with $I_0(x) = J_0(ix)$, B a constant which depends on how much the nucleon density on the surface of the nucleus is larger than in its center, and the corresponding scattering amplitude

$$f(q) = e^{-Bq^2} J_0(qR) \tag{3.14}$$

3.3 Regge-Theory and Pomeron Exchange

Diffractive dissociation can be considered to be an interaction with a pomeron $\mathbb{P}$ as exchange particle. Regge Theory provides a relation between the masses and

$\pi \bigoplus \mathbb{P}$	
$1^-(0^{-+}) \bigoplus 0^+(2^{++})$	
0^+	$1^-(2^{-+})$
1^-	$1^-(1^{++}, 2^{++}, 3^{++})$
2^+	$1^-(0^{-+}, 1^{-+}, 2^{-+}, 3^{-+}, 4^{-+})$
l^P	$I^G(J^{PC})$

Table 3.1: Fusion process of an incoming pion with a pomeron [Chu05]

spins of particles (see figure 3.2), where the different resonances show a linear relation of the masses and spins. The pomeron is a tensor glueball and therefore a $J^{PC} = 2^{++}$ object[2]. Depending on the relative angular momentum l^P between the pomeron and the incident hadron h (cf. figure 3.1), the created state can hold different J^{PC}. For an incident pion ($I^G(J^{PC}) = 1^-(0^{-+})$), this correlation is exemplified in table 3.1. The potential relative angular momenta l^P of the fusion process which is shown in the first line, are listed on the left side. The possible resulting quantum numbers are assigned to them on the right side.

[2]In the following the notation $I^G(J^{PC})$ is used to determine the quantum numbers of a particle, with I the isospin, G the G-parity, J the total angular momentum, P the parity and C the C-parity [PDG04].

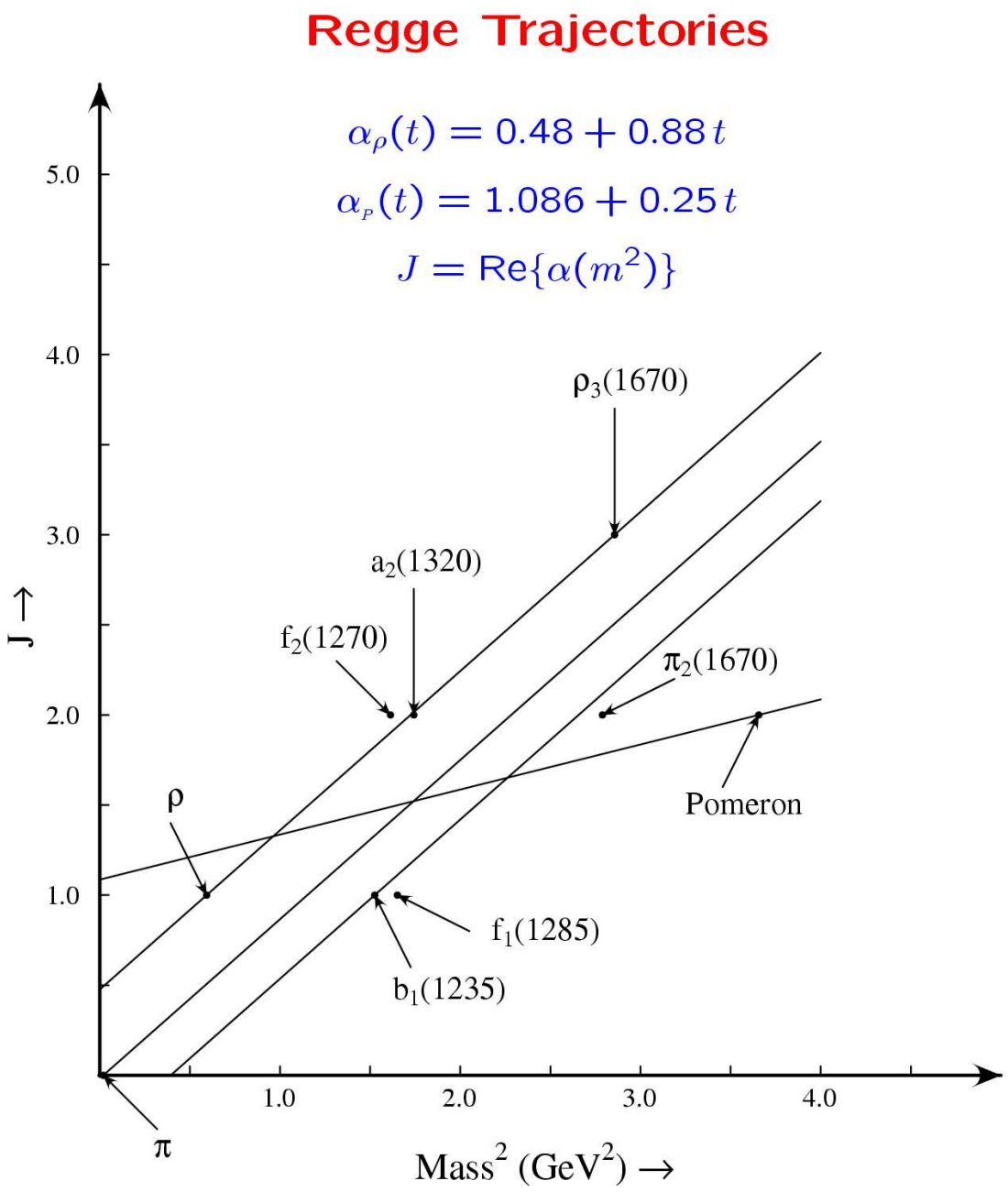

Figure 3.2: Regge trajectories (from [Chu05], for explanation see text)

Chapter 4

Three-Body Decays

The momenta of decay products are usually not distributed isotropically with reference to the rest system of the parent resonance. The occuring angles depend on the spins of the involved particles and the angular momenta created within the decay. The main task here is to figure out spins and parities of the resonances from the angular distributions of the decay particles. To get a rough impression of the contributing angular momenta of the parent state of a three-body decay, Wigner D-Functions and Moments of the decays have to be calculated.
The Euler Angles α, β and γ, which describe the position of the decay plane in the rest system of the parent state, are introduced in section 4.1. Section 4.2 gives an overview of the method of investigating the occuring angular distributions by calculating the unnormalized moments.

4.1 Calculation of the Euler Angles

Considering a system of three particles 1, 2, 3, with $\vec{p}_i$ the momentum of particle i, one can define a "standard orientation" of this system in its rest frame. This coordinate system is body-fixed. Its y-axis is defined[1] along the opposite direction of $\vec{p}_1$, while the z-axis is along $\vec{p}_2 \times \vec{p}_3$. A rotation to a system with arbitrary orientation can be described by the Euler Angles α, β and γ.
For calculating these angles for a three-particle system, one starts in the Jackson Frame, that means in the rest frame of the parent state, with the $\hat{z}_J$-axis along the direction of the initial (beam) particle and the $\hat{y}_J$-axis perpendicular to the

[1] in the following text is assumed that particles 2 and 3 are indistinguishable (e.g. π^-), while particle 1 is a different one (e.g. π^+)

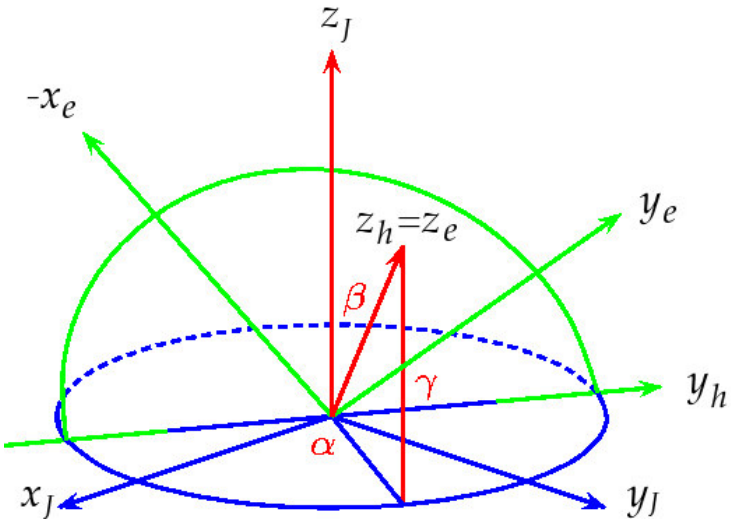

Figure 4.1: Calculation of the Euler Angles (adapted from [Chu05])

production plane. The decay plane in Jackson Frame is given by its normal

$$\vec{n} = \frac{\vec{p}_2 \times \vec{p}_3}{|\ \vec{p}_2 \times \vec{p}_3\ |} \tag{4.1}$$

what α and β are calculated from[2]:

$$\alpha = \text{atan2}(n_y, n_x) \tag{4.2}$$

$$\beta = \arccos n_z \tag{4.3}$$

The Helicity Frame (convention as used e.g. by S. U. Chung [Chu05]) is given by

$$\hat{z_h} = \vec{n} \tag{4.4}$$

$$\hat{y_h} = \hat{z_J} \times \hat{z_h} \tag{4.5}$$

$$\hat{x_h} = \hat{y_h} \times \hat{z_h} \tag{4.6}$$

For calculating the third angle γ the Euler Frame is also necessary

$$\hat{z_e} = \hat{z_h} \tag{4.7}$$

$$\hat{y_e} = -\frac{\vec{p}_1}{|\ \vec{p}_1\ |} \tag{4.8}$$

$$\hat{x_e} = \hat{y_e} \times \hat{z_e} \tag{4.9}$$

[2]the function atan2(,) is understood in the following to be such that the angle ϕ is always referring to the correct quadrant

so that γ is given by

$$\gamma = \text{atan2}(\hat{x_e} \cdot \hat{y_h}, \hat{y_e} \cdot \hat{y_h}) \tag{4.10}$$

4.2 Angular Distributions

4.2.1 Basic Principles

For a reaction

$$A + B \rightarrow X + C \tag{4.11}$$

$$X \rightarrow 1 + 2 + 3 \tag{4.12}$$

the interaction matrix element is given by

$$\mathcal{M}(R) = \sum_a V_a \mathcal{D}_a(R) \tag{4.13}$$

V_a is the production amplitude of this process[3] and $\mathcal{D}_a$ the decay amplitude, with the parameters $R = (\alpha, \beta, \gamma)$ and $a = (J, m, \mu, \eta)$, with J the angular momentum of the parent particle X, m the projection of J to the space-fixed z-axis, μ the rotationally invariant z-component for the body-fixed axes and η the intrinsic parity. This corresponds to the angular distribution

$$I(R) \sim \frac{d\sigma}{dR} \sim \sum_{aa'} V_a V_{a'}^* \mathcal{D}_a \mathcal{D}_{a'}^* \tag{4.14}$$

The decay amplitude (cf. [Chu71], Chapter 6) depends on the helicity coupling amplitude $F^{J\eta}$

$$\mathcal{D}_a(R) \sim F_\mu^{J\eta}(m_{12}^2, m_{13}^2) D_{m\mu}^{J*}(\alpha, \beta, \gamma) \tag{4.15}$$

which is a function of the invariant masses of the two-body-subsystems, m_{12}^2 and m_{13}^2, and the D-Function $D_{m\mu}^J$ which gives the appropriate angular dependence on the Euler Angles.
So the angular distribution can also be written as

$$I(R) \sim \sum_{Jm\mu J'm'\mu'} V_a V_{a'}^* D_{m\mu}^{J*} D_{m'\mu'}^{J'} F_\mu^{J\eta} F_{\mu'}^{J'\eta'*} \tag{4.16}$$

[3] assuming that the initial and final states of the collision partner, B and C, have spin 0

4.2.2 Helicity Coupling Amplitude

Assuming parity conservation, the relation

$$F_{\mu}^{J\eta} = \eta(-)^{\mu+1} F_{\mu}^{J\eta} \tag{4.17}$$

gives the intrinsic parity of the parent state

$$\eta = (-)^{\mu+1} \tag{4.18}$$

From the indistinguishability of particle 2 and 3 follows

$$F_{\mu}^{J\eta}(m_{12}^2, m_{13}^2) = (-)^{J+\mu} F_{-\mu}^{J\eta}(m_{13}^2, m_{12}^2) \tag{4.19}$$

4.2.3 Wigner D-Functions

The elements of the Rotation Matrix are (following Wigner's convention, cf. [Ros57], p. 51f)

$$D_{m\mu}^{J} = \langle JM \mid e^{-iJ_z\alpha} e^{-iJ_y\beta} e^{-iJ_z\gamma} \mid J\mu \rangle \tag{4.20}$$

$$= e^{-im\alpha} \langle Jm \mid e^{-iJ_y\beta} \mid J\mu \rangle e^{-i\mu\gamma} \tag{4.21}$$

$$= e^{-im\alpha} d_{m\mu}^{J}(\beta) e^{-i\mu\gamma} \tag{4.22}$$

The following expression for $d_{m\mu}^{J}$ has been given by Wigner:

$$\begin{aligned} d_{m\mu}^{J}(\beta) = {} & [(J+\mu)!(J-\mu)!(J+m)!(J-m)!]^{1/2} \\ & \times \sum_{\kappa} \frac{(-)^{\kappa}}{(J-m-\kappa)!(J+\mu-\kappa)!(\kappa+m-\mu)!\kappa!} \\ & \times \left(\cos\frac{\beta}{2}\right)^{2J+\mu-m-2\kappa} \left(-\sin\frac{\beta}{2}\right)^{m-\mu+2\kappa} \end{aligned} \tag{4.23}$$

where the sum is over the values of the integer κ for which the factorial arguments are greater than or equal zero ([Ros57], p. 53).
The D-Functions are normalized and orthonormal (cf. [Chu71], Appendix A)

$$\int dR\; D_{m_1\mu_1}^{J_1 *}(R) D_{m_2\mu_2}^{J_2}(R) = \frac{8\pi^2}{2j_1+1} \delta_{j_1 j_2} \delta_{m_1 m_2} \delta_{\mu_1\mu_2} \tag{4.24}$$

and they statisfy the following coupling roule:

$$D_{m_1\mu_1}^{J_1} D_{m_2\mu_2}^{J_2} = \sum_{j_3 m_3 \mu_3} (J_1 m_1 J_2 m_2 \mid J_3 m_3)(J_1\mu_1 J_2\mu_2 \mid J_3\mu_3) D_{m_3\mu_3}^{J_3} \tag{4.25}$$

From the two equations above, there follows the useful relation

$$\int dR D^{J_1}_{m_1\mu_1}(R) D^{J_2}_{m_2\mu_2}(R) D^{J_3 *}_{m_3\mu_3}(R) =$$

$$= \frac{8\pi^2}{2j_3+1}(J_1 m_1 J_2 m_2 |\ J_3 m_3)(J_1\mu_1 J_2\mu_2 \mid J_3\mu_3) \tag{4.26}$$

In this notation, the Clebsch-Gordan-Coefficient describes the coupling of J_1 and J_3 to J_2, etc [Chu05].

4.2.4 Moments

The moments of the angular distributions $D^L_{MN}(\alpha,\beta,\gamma)$ are connected to the production amplitudes V_a

$$H(LMN) = \langle D^L_{MN}(\alpha,\beta,\gamma)\rangle \tag{4.27}$$

$$= \int dR\, I(R) D^L_{MN}(R) \tag{4.28}$$

$$\sim \int dR \sum_{aa'} V_a V^*_{a'} F^{J\eta}_{\mu} F^{J'\eta' *}_{\mu'} D^{J*}_{m\mu}(R) D^{J'}_{m'\mu'}(R) D^L_{MN}(R) \tag{4.29}$$

$$= \sum_{aa'} V_a V^*_{a'} \frac{F^{J\eta} F^{J'\eta' *}}{2J+1}\ (J' m' LM \mid Jm)(J'\mu' LN \mid J\mu) \tag{4.30}$$

where 4.26 was used in the last step.
This corresponds to the selection criteria for spins: The quantum numbers (J, m, μ) and (J', m', μ') can contribute to an observed resonance with (L, M, N) only if the Clebsch-Gordan coefficients are not zero.
From the definition of the moments follows the constraint

$$H^*(LMN) = (-)^{M-N} H(L\ -M\ -N) \tag{4.31}$$

Assuming parity conservation in production and decay, it can be shown

$$H(LMN) = (-)^{L+M+N} H(L\ -M\, N) \tag{4.32}$$

So it follows that

$$H^*(LMN) = (-)^{L} H(LM\ -N) \tag{4.33}$$

It is sufficient to consider moments with positive values for M as well as N, as the moments for negative values can be obtained from them uniquely.
Particle exchange of the indistinguishable particles 2 and 3 of integer spins leads

to the relation (see [Chu71] and [ChT75] for details):

$$H^*(LMN;m_{12},m_{13}) = (-)^L H(LMN;m_{13},m_{12}) \tag{4.34}$$

$$= \left\{ \begin{array}{ll} \text{real} & \text{for } L = \text{even} \\ \text{imaginary} & \text{for } L = \text{odd} \end{array} \right\} \tag{4.35}$$

so that parity conservation can obviously be seen in a data sample if this relation holds.
The normalized angular distribution $I(R)$ is connected to the moments by

$$I(R) = \sum_{LMN}^{L_{max}} \frac{2L+1}{8\pi^2} H(LMN) D^{L*}_{MN}(R) \tag{4.36}$$

meaning that the $H(LMN)$ determines the weight of the quantum numbers LMN in the series expansion of $I(R)$ in the D^L_{MN} base. L_{max} depends of the mass m_X, as there is a maximum value for the spin of a resonance of a certain mass, e.g. with 1.5 GeV the maximum spin is 2.
With the set of $\{H\}$ the angular distribution is fixed, so that from the knowledge of the contributing Hs one gets complete knowledge of the contributing spins.

4.2.5 Unnormalized Moments

What can be measured experimentally, are the unnormalized moments, defined as

$$h(LMN) = n\ H(LMN) = \sum_{i=1}^{n} D^L_{MN}(\alpha_i, \beta_i, \gamma_i) \tag{4.37}$$

with the corresponding error bars

$$[\delta\{\mathrm{Re}(h(LMN))\}]^2 = \sum_{i=1}^{n} [\mathrm{Re}(D^L_{MN}(\alpha_i, \beta_i, \gamma_i))]^2 \tag{4.38}$$

$$[\delta\{\mathrm{Im}(h(LMN))\}]^2 = \sum_{i=1}^{n} [\mathrm{Im}(D^L_{MN}(\alpha_i, \beta_i, \gamma_i))]^2 \tag{4.39}$$

where n is the number of events in a given bin of the total mass of the parent state m_X.
One considers the sum of the moments, as signal and background are additive and from the sum the background can be subtracted easily, what would be disturbed by a division by n.
To get a correct physics result, one also needs to correct for the acceptance of the

experimental setup.
For the unnormalized moments unequal zero, one can learn from the Clebsch-Gordan coefficients that the spins J and J' of the contributing resonances follow the selection criteria

$$
\begin{aligned}
|\, J - J' \,| \leq L \leq J + J' \\
M = m' - m \\
N = \mu' - \mu
\end{aligned}
\tag{4.40}
$$

Chapter 5

Results from Previous Experiments

Investigations of the dissociation of π^- into three charged π^- on nuclear targets

$$\pi^- A \rightarrow \pi^+ \pi^- \pi^- A \tag{5.1}$$

as presented in chapter 6, have been performed at the VES[1] and at BNL[2] already some years ago with lower energies. Their results are briefly discussed in this chapter.

5.1 Results from the VES Experiment

The VES collaboration performed a partial wave analysis on 3π systems in the reaction $\pi^- A \rightarrow \pi^+ \pi^- \pi^- A$ at the momentum 36.6 GeV/c on a beryllium target. The analyzed statistics contained $0.8 \cdot 10^6$ events.
The partial wave analysis was performed in the mass region $0.8 - 2.6\,\mathrm{GeV}$ for different t regions between $0.010\,(\mathrm{GeV}/c)^2 \leq t \leq 0.800\,(\mathrm{GeV}/c)^2$. The system $\rho\pi$ with the exotic quantum numbers $J^{PC} = 1^{-+}$ is investigated. No narrow exotic object in the mass region $m \approx 1.6\,\mathrm{GeV}$ is found, which could indicate the $\pi_1(1600)$.
The analysis was done with a new type of amplitude analysis, the extraction of the largest eigenvalue of the density matrix. An outline of this method and the results can be found in [Kac02].

[1] **VE**rtex **S**pectrometer (at Protvino, Russia)
[2] **B**rookhaven **N**ational **L**aboratory (USA)

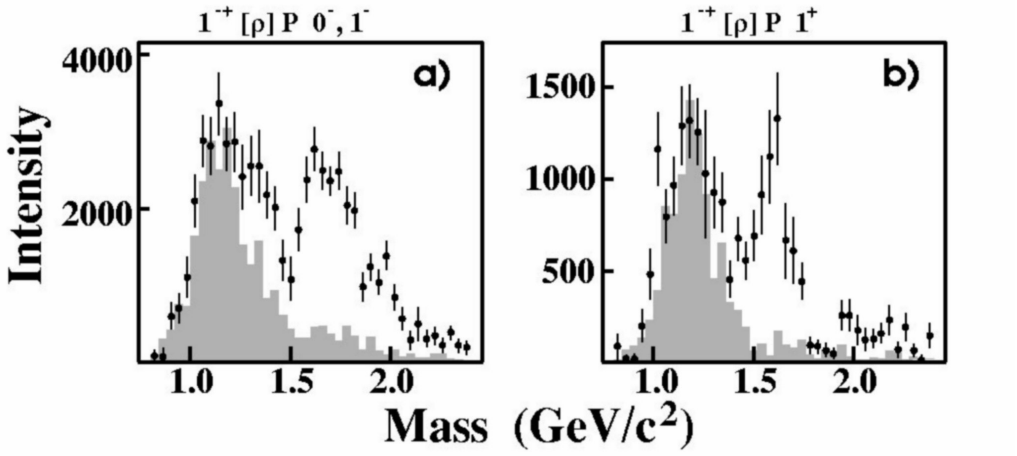

Figure 5.1: Wave intensities of the 1^{-+} exotic wave in BNL-E852 (from [Chu02])

5.2 Results from BNL-E852

The experiment E852 at BNL studied the reaction $\pi^- p \rightarrow \pi^+\pi^-\pi^- p$ with momenta of 18 GeV/c. The primary goal was the search for exotic mesons. A partial wave analysis was performed on a data sample of 250 000 events.
The well-known states $a_1(1260)$, $a_2(1320)$ and $\pi_2(1670)$ were observed. Additionally the 0^{-+} $\pi(1300)$, the 0^{-+} $\pi(1800)$, the 1^{++} $a_1(1700)$, the 3^{++} a_3 state and the 4^{++} $a_4(2040)$ have been found in one or more of the decay channels $\rho\pi$, $f_0(980)\pi$, $\sigma\pi$, $f_2\pi$ and $\rho_3\pi$.
The exotic $J^{PC} = 1^{-+}$ $\rho\pi$ wave shows indications of the $\pi_1(1600)$ resonance: A state with a resonance mass of $1593 \pm 8^{+29}_{-47}$ GeV and a width of $168 \pm 20^{+150}_{-12}$ MeV is observed. Its shape and width are strongly dependent of the model used for the partial wave analysis.
Figure 5.1 presents the wave intensities of the 1^+ $[\rho]$ P exotic waves. The 21-wave rank-1 partial wave analysis fit of the data is shown as the points with error bars. The shaded histograms show estimated contributions from all non-exotic waves due to leakage. For more information on this analysis, see [Chu02].

Chapter 6

Data Analysis

A major part of the COMPASS hadron physics program (see section 2.1.2) is the investigation of the diffractive dissociation (cf. chapter 3) of high energy pions, kaons, and protons. In autumn 2004, a first hadron beam time [Fer05] with a 190 GeV π^- beam on lead, copper and carbon targets took place with about one week of commissioning and two weeks of physics data taking.
In this chapter an elementary analysis of the diffractive dissociation

$$\begin{aligned} \pi^- + Pb &\to X^- + Pb \\ X^- &\to \pi^+ + \pi^- + \pi^- \end{aligned} \tag{6.1}$$

is presented. Section 6.1 introduces some physical assumptions made in the analysis of this process and some constraints due to the experimental setup and the data available at the time when this thesis is written. The selection criteria whether an event is supposed to be a *diffractive* one of type (6.1) (i.e. the cuts in energy, vertex, momentum transfer and triggers) are described in section 6.2. Subsequently the resulting mass spectra, angular distributions and unnormalized moments are presented in section 6.3.

6.1 Basic Conditions

The underlying investigated process (6.1) is pictured in figure 6.1. The 190 GeV π^- grazes the lead target nucleus, is excited to an intermediate state X^- and decays into three charged pions (one π^+, two π^-) which are all detected in the spectrometer and whose laboratory momenta are measured.
The real experiment does not have perfect conditions and setup, but is limited due to technical reasons, with relevant influence on the data analysis:

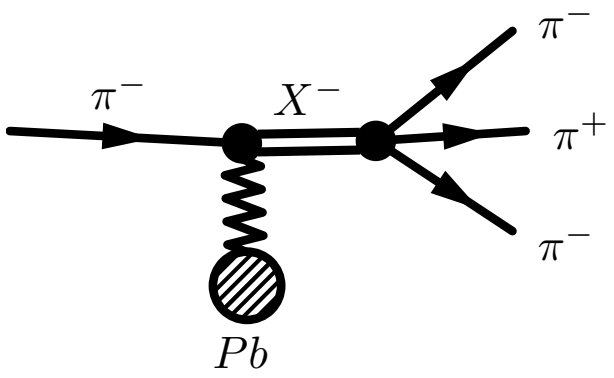

Figure 6.1: The reaction $\pi^- + Pb \rightarrow \pi^+ + \pi^- + \pi^- + Pb$

- The energy of the beam particles is not measured, and their nature is not identified. The so-called *pion beam* consists mainly of pions, but has a small contamination of kaons ($\sim$ 4.5%) and anti-protons ($\sim$ 0.5%) [Fer05]. Unfortunately the CEDARs (see section 2.2.3), which were supposed to tag the kaons in the beam by their different Cherenkov ring (compared to pions) did not work in 2004. Therefore, the only beam property which is really measured is the direction of the beam particles which can be reconstructed on the basis of the hits in the silicon detectors in front of the target.

- The nature of the outgoing particles is not determined. The RICH (section 2.2.3) which is used to identify particles after the first spectrometer magnet in muon program was switched off on purpose for the hadron beam. The three-momenta of the outgoing particles are reconstructed by the tracking procedure in CORAL (section 2.3.2). The energy deposited by the particles in the calorimeters is not sufficiently accurate measured to conclude from the calculated mass region to a certain particle identity. The fraction of energy of a particle which is deposited in ECAL is supposed to peak at $\frac{E_{ECAL}}{E_{particle}} \approx 1$ for photons and electrons, and therefore allow to extract or exclude them. In the data of the first hadron beam time no such peak can be seen, so that no meaningful cut in the kind of interaction of particles can be applied.

- A limitation for the analysis of diffractive processes can be the trigger assortment in the first hadron beam time in 2004. There are two special triggers designed for being activated with diffractive events. One of them was not switched on for the whole beam time, the other one only for a part. In data taken during the time with this trigger, the ratio of candidates for

diffractive events is about one and a half as large as without it (cf. section 6.2.5).

The analysis presented in this thesis is based on mDST-files which are processed by PHAST (see section 2.3.3) and afterwards visualized by ROOT (section 2.3.1). During the hadron run about 200 runs[1] with a data quality sufficient for analysis were taken (cf. section 7). Directly after the hadron beam time the first mDSTs of some chunks[2] of some runs were produced, the so-called *November pre-production* of 2004, on which the principles of this analysis were performed preliminary. In the meantime several improvements in tracking and vertexing algorithms and in the alignment procedure were done, as well as recalibrations of several detectors (silicons and ECAL) and a new trigger calibration. The production of high statistics with revised parameters was started four weeks before this thesis is finished. The analysis on hand is based on 855 (out of a total number of 897) chunks of three runs with two sorts of lead targets of varied thickness and two different trigger sets. This is all statistics with hadron beam and lead target[3] which was available until December 2nd.

6.2 Event Selection

The analyzed data sample contains in total 37 471 123 events, which can have very different character (concerning e.g. the amount and quality of reconstructed tracks and vertices or deposited energy in the calorimeters). So obviously not every one of them is supposed to have a signature that fits process (6.1). In this section the cuts applied on the data sample to get only events which are good candidates for a diffractive dissociation of this kind are introduced.

6.2.1 Three Charged Particles

The first obligatory constraint for a good candidate is the requirement of exactly three charged outgoing particles. So only events with a vertex with incoming

[1] A run is a COMPASS-internal unit of data-taking, which lasts about an hour and contains up to 200 spills. A spill is a 4.8 seconds lasting time window where the particles arrive at the COMPASS spectrometer, followed by a short break of 12 seconds due to the SPS cycle.

[2] A chunk is a unit of data which is created during the process of data acquisition. It is limited to the maximum raw data file size of 1 GB and contains about 50 000 events.

[3] In addition there were some chunks of a run with "empty target" and some chunks of a run with muon beam and hadron setup produced, for comparison issues. This data is not used in this analysis. No chunks of runs with carbon or copper targets were produced up to now, though such data were taken.

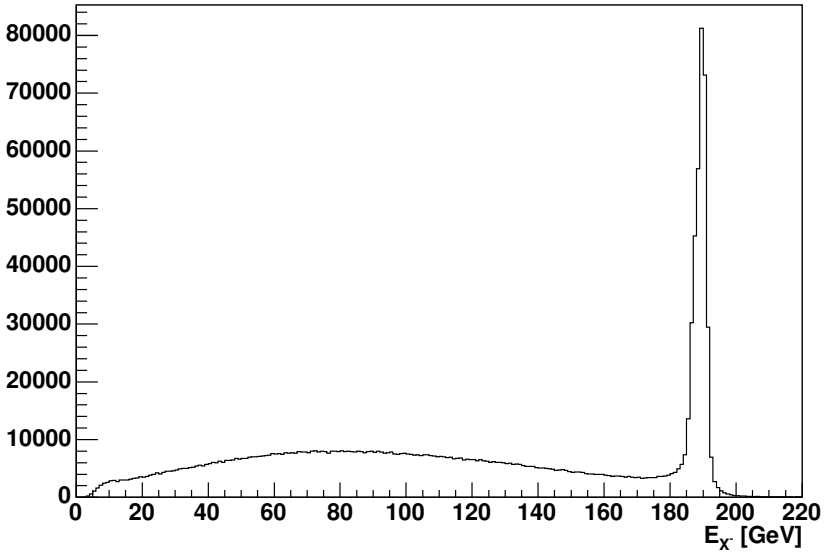

Figure 6.2: Energy distribution of the three-pion system

beam particle and one positive and two negative outgoing particles enter the further analysis. This reduces the data sample to 1 372 620 events.

6.2.2 Energy Distribution

In a second step the total energy of the $\pi^+\pi^-\pi^-$ system X^-, which is supposed to be equal the beam energy within the accuracy of the experiment, is considered. As noted in section 6.1, the nature of the beam particles is not ensured, so in this analysis it is assumed that they are all pions.
The energy of each of the outgoing particles is calculated with the measured three-momentum vector and the assumption that these particles are indeed pions. In the beginning of the analysis procedure, also the two assumptions

$$X^- \to \pi^- + K^+ + K^- \tag{6.2}$$

$$\text{and} \quad X^- \to \pi^- + e^+ + e^- \tag{6.3}$$

were tested with intend to exclude these processes. In the non-exclusive mass spectrum of the electron-electron subsystem a clear peak at $m_{e^+e^-} = m_\gamma = 0$ could be seen, but after the cuts on vertex and momentum transfer (see sections 6.2.3 and 6.2.4) were applied, it disappeared, so that the contribution of this decay is not significant. The kaon-kaon subsystem was checked for contributions of $m_{K^+K^-} = m_\Phi$, but neither this resonance nor another sharp one could be seen

significantly. The energy of X^-, E_{X^-}, is then given by the sum of the three single energies which can be seen in figure 6.2. A clear peak at $E_{X^-} = 189\,\text{GeV}$ can be seen, with $\sigma \approx 1.7\,\text{GeV}$ which can be traced back to the momentum spread of the beam ($\approx 0.7\%$).
Furthermore the measurement is expected to be exclusive, that means that all created particles or their decay products, respectively, are detected within the spectrometer. This means that $E_{X^-} = E_{beam} - E_{trans}$, with E_{beam} the energy of the incident particle and E_{trans} the energy transferred from the incident particle to the target nucleus. As for diffractive scattering the square momentum transfer t is small and the recoil partner, the lead nucleus, has an invariant mass $m_{Pb} \approx 193\,\text{GeV}$, $E_{trans} = \frac{|t|}{2m_{Pb}}$ can be estimated to be negligible with respect to the resolution of the spectrometer. So $E_{X^-} = E_{beam}$ if all preconditions of the diffractive process (6.1) are fulfilled. In other words, based on the distribution of the total energy an energy-cut on the data sample can be applied. The band $E_{X^-} = 189 \pm 4\,\text{GeV}$ selects 336 768 events in the peak region out of the three-particle sample.
As can be seen from the plot, this selection is rather clean but not 100% pure. Extrapolating the broad non-exclusive spectrum at lower energies, a contamination of the order of 10% of non-exclusive processes is to be expected within this exclusivity cut. This is neglected in the following considerations.

6.2.3 Vertex Distribution

The distribution of the vertices of the exclusive three-particle events is presented in figure 6.3. The region around the target is displayed along the beam axis (corresponding to the z-axis of the COMPASS MRS[4]). Dominant sharp peaks can be seen at the positions of the target and the scintillator which is also called Multiplicity Counter. Smaller, but still noticeable peaks appear at the locations of the beam counter and silicon stations. The triple structure of the target results from different lead targets which were used. There was a 3 mm disk as well as a divided target which consisted of two disks, 1 and 2 mm thick. All this data is treated altogether in this analysis.
The ratio between vertices in the target and vertices in the air around the target is reasonable. The diffractive cross section scales with R^2 and $A^{2/3}$, respectively. This has to be multiplied with the number of atoms, which can be calculated from the densities ($\rho_{Pb} = 11.3\ \text{g/cm}^3$, $\rho_{air} = 1.2 \cdot 10^{-3}\ \text{g/cm}^3$ divided by the atomic

[4]Main Spectrometer Reference System: right-handed system with $\hat{z}$ along beam and $\hat{y}$ vertical with origin in the center of the polarized target of the muon program

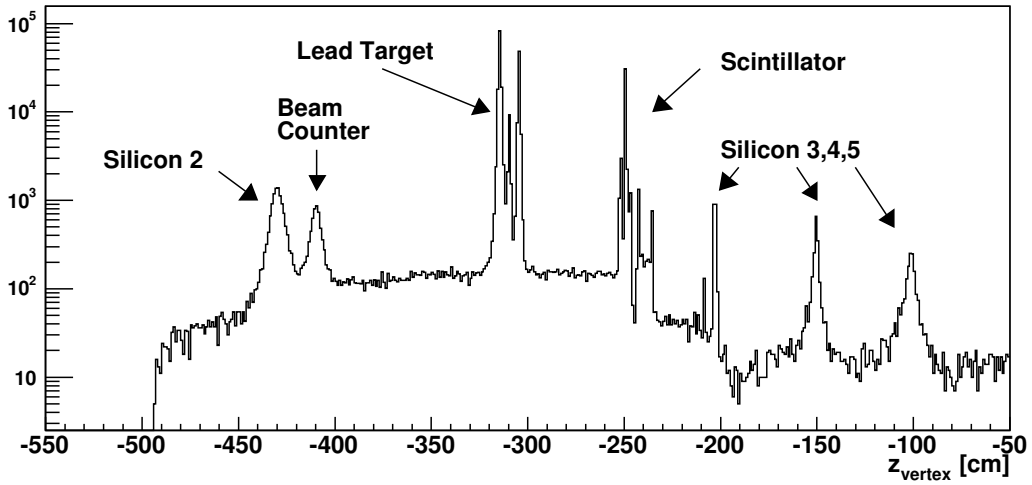

Figure 6.3: Vertex distribution for exclusive events

masses, so that the ratio between the vertices is theoretically given by

$$\frac{n(z_{vertex}, Pb)}{n(z_{vertex}, air)} = \frac{A_{Pb}^{-1/3} \cdot \rho_{Pb}}{A_{air}^{-1/3} \cdot \rho_{air}} \approx 3800 \tag{6.4}$$

The experimental ratio $\frac{n(z_{vertex},Pb)}{n(z_{vertex},air)}$, standardized to 3 mm thickness, is given by 5 100 for exclusive events, what is in the same order of magnitude.
For further analysis cuts on the lead target in $z_{vertex} = -309.5 \pm 10$ cm were applied, so that 203 587 events remained. For comparison purposes in section 6.2.4 exclusive three-particle events with vertex in the scintillator ($z_{vertex} = -242 \pm 10$ cm, 42 031 events) and vertex in a silicon detector ($z_{vertex} = -200 \pm 10$ cm, 2 315 events) are chosen.

6.2.4 t-Distribution

The squared four-momentum transfer t from the beam to the target nucleus is given by (3.2). As mentioned in section 6.1, energy and momentum of the beam are not measured. All calculations start with the assumption that the magnitude of the beam momentum is exactly 190 GeV/c. This has to be corrected by a scaling factor

$$corr = \frac{|\vec{p}_{X^-}|}{190\,\mathrm{GeV}/c} = \frac{\sqrt{E_{X^-}^2 - m_{\pi^-}^2}}{190\,\mathrm{GeV}/c} \tag{6.5}$$

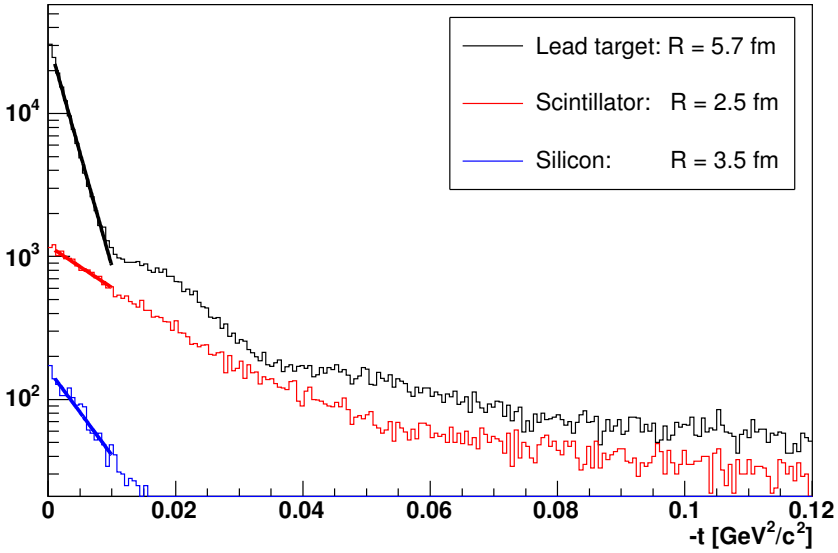

Figure 6.4: Momentum transfer on different "target" materials

whereby an exclusive diffractive process is assumed. Now iteratively the beam energy and the momentum transfer can be calculated more accurately. In this case it turned out that the first correction of the momentum components of the beam Lorentz vector with (6.5) is sufficiently accurate.
Figure 6.4 presents the magnitude of the squared momentum transfer, $-t$, of exclusive three-particle events on the lead target, on the scintillator and on silicon. The diffractive patterns of the different nuclei can be seen. The cross section of the lead target shows the first diffraction minima and maxima quite clearly. The slope b of the logarithm of the differential cross section near zero gives the radius R of the diffracting core by (3.12), so that one obtains $R = 5.7\,\text{fm}$ for lead, $R = 2.5\,\text{fm}$ for the scintillator material, and $R = 3.5\,\text{fm}$ for silicon. These values meet approximately the ones derived from the correlation $R = R_0 A^{1/3}$, A the mass number of an element, $R_0 \approx 1\,\text{fm}$.
To select the events with small momentum transfer, but concurrently exclude events with electromagnetic interaction and therefore $t \approx 0$, the band $0.001\,(\text{GeV}/c)^2 < -t < 0.01\,(\text{GeV}/c)^2$ defines a good cut which selects 188 929 events from the initial sample. As can be seen from the Primakoff analysis, the experimental resolution for t is better than $0.001\,(\text{GeV}/c)^2$. The energy distribution for events selected by this cut is presented in figure 6.5. If here the non-exclusive part of the spectrum is extrapolated to the exclusive peak, the contamination with non-exclusive events is smaller than one percent. Then for the analysis of process (6.1) 99 749 exclusive three-particle events with small momentum transfer and

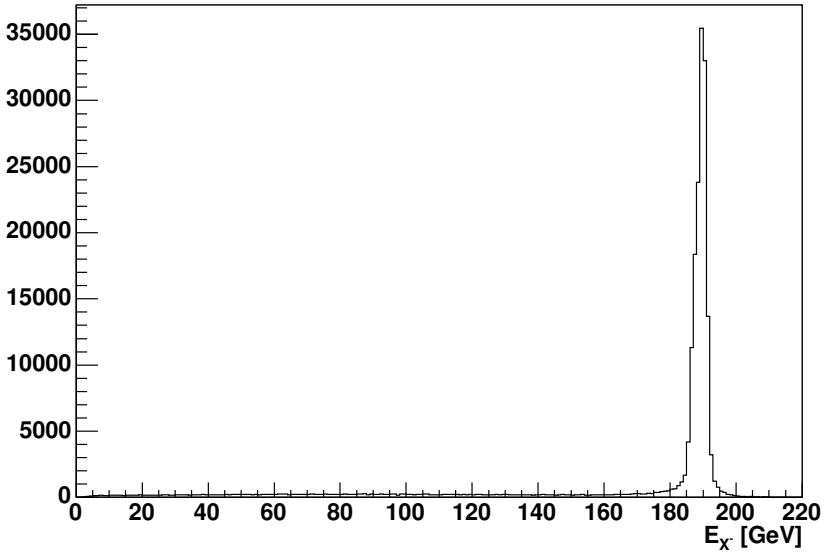

Figure 6.5: Energy distribution for events with small momentum transfer

vertex in the lead target remain.

6.2.5 Triggers

In the analysis on hand, no cuts on triggers were applied. For the preliminary analysis, the main reason was that during the time when about 60% of the analyzed statistics were taken, the dedicated diffractive trigger was switched off. For the statistics with this trigger switched on, comparisons showed that the cuts in energy and momentum transfer resulted in the same signature of mass spectra. More than 99% of the remaining events are taken with diffractive trigger. So a cut on this trigger seems not to be demanded. On the other hand, the analysis of the data with diffractive trigger shows that the fraction of three-particle events is increased by a factor 1.6 compared to data taken without diffractive trigger (cf. section 7.2).

6.3 Mass Spectra and Angular Distributions

From the data sample which contains only events which are selected to be adequate the diffractive dissociation process (6.1) the mass spectrum of the $\pi^+\pi^-\pi^-$ system as well as the Dalitz plot for the two-pion subsystems are shown in this

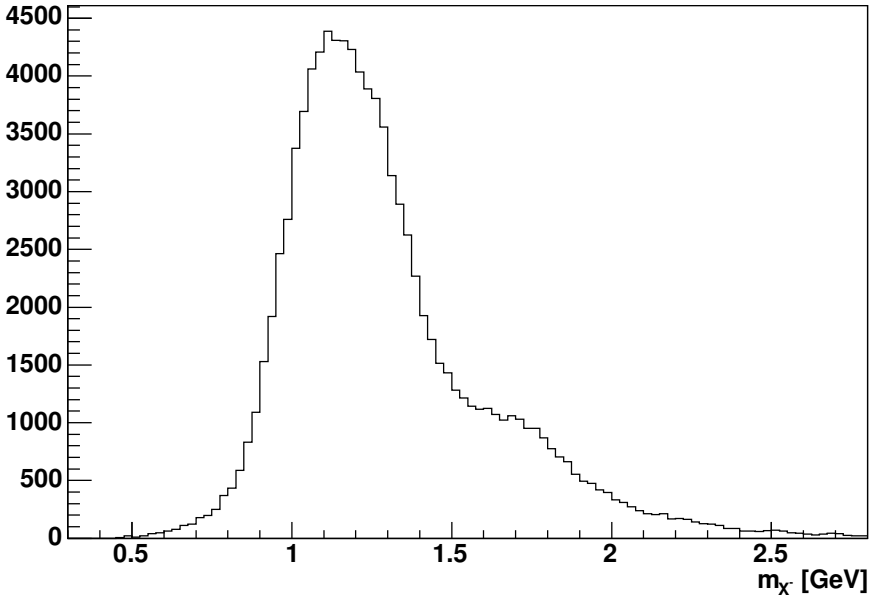

Figure 6.6: Total mass of the $\pi^+\pi^-\pi^-$ system

section. Furthermore, the distributions of the Euler Angles of the decay process and the most significant unnormalized moments, which point out the spins the intermediate state can adopt, are presented.

6.3.1 Total Mass Distribution

The invariant mass m_{X^-} of the three-pion system X^-

$$X^- \rightarrow \pi^+ + \pi^- + \pi^- \tag{6.6}$$

is obtained from the sum of the Lorentz vectors of the three outgoing pions. Its spectrum is revealed in figure 6.6. A significant peak can be seen at $m_{X^-} \approx 1.15\,\mathrm{GeV}/c^2$, with an apparent shoulder at $m_{X^-} \approx 1.3\,\mathrm{GeV}/c^2$. Additionally a slight peak is located at $m_{X^-} \approx 1.7 - 1.8\,\mathrm{GeV}/c^2$.

6.3.2 Dalitz Plot

If a decay process has three particles in the final state, as e.g. (6.1), phase space is characterized by 12 parameters (according to the 3 four-momenta). Three of them are defined by the masses of the three particles, which are assumed to be pions

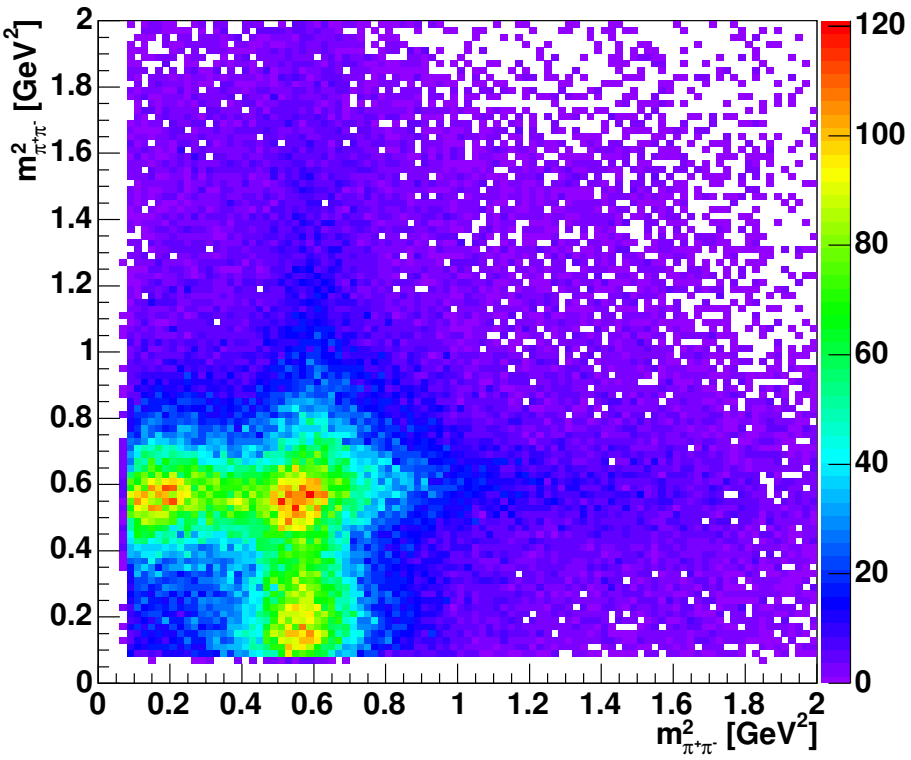

Figure 6.7: Dalitz plot for the $\pi^+\pi^-$ pairs

in this analysis. Four parameters are determined by energy and momentum conservation. So the process features five independent parameters.
Those are the three Euler angles (see section 4.1 and section 6.3.3) and two invariant masses m^2_{ij} of different pairs of particles in the final state.
The invariant masses of two different two-particle combinations can be plotted versus each other in a Dalitz plot. In this analysis the Dalitz plot of the two $\pi^+\pi^-$ subsystems is presented in figure 6.7. Which π^- is supposed to contribute to which subsystem (i.e. at which subsystem's axis it is plotted) is chosen randomly, reflecting the indistinguishability of the two π^-.
In the Dalitz plot the two bands of the $\rho(770)$-decay

$$\rho \rightarrow \pi^+ + \pi^- \tag{6.7}$$

are clearly visible at $m^2_{\pi^+\pi^-} = m^2_\rho \approx 0.6\,\mathrm{GeV}^2$, with a maximum at the $\rho - \rho$ interference. Apart from them, no significant resonances can be extracted from the Dalitz plot without higher statistics and further analysis of angular distributions.

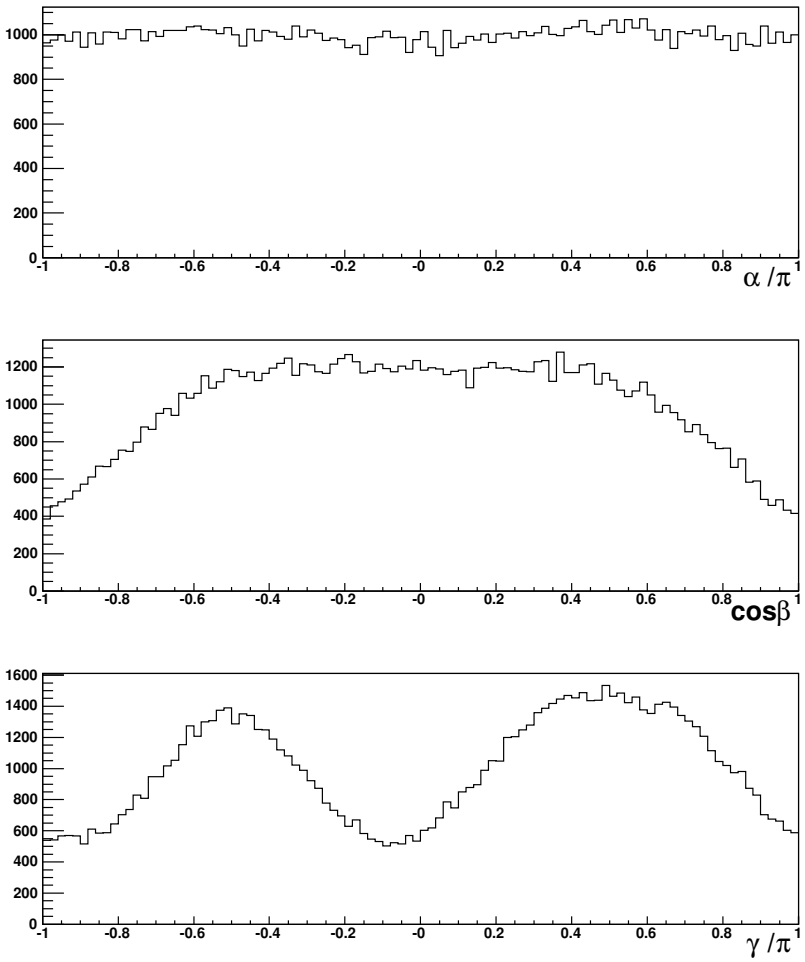

Figure 6.8: Measured Euler Angles of the decay

6.3.3 Angular Distributions

The three Euler Angles α, β and γ (see section 4.1) describe the position of the decay plane of the three pions in the rest system of the parent state X^-. Without polarization of the X^- the decay should be arbitrarily orientated in space and the angles therefore distributed flat.
The angular distributions extracted from the data sample of the diffractive three-pion dissociation are presented in figure 6.8. The α-distribution is smooth, analogical the $\cos\beta$-distribution, whose gradient boundaries probably result from acceptance problems. The γ-distribution provides a structure whose origin could not be assessed up to now, but which if hoped to be clarified after acceptance corrections.
The correlations between α, $\cos\beta$ and γ can be seen in figure 6.9. The correlations

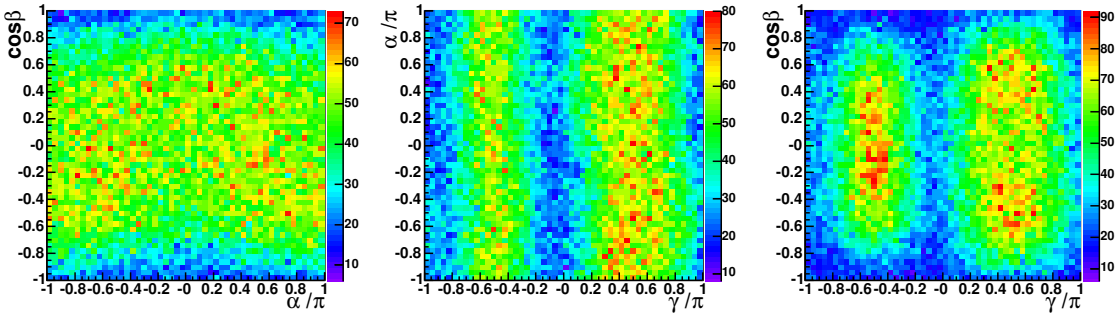

Figure 6.9: Correlations between α, cosβ and γ

$\alpha - \cos\beta$ and $\alpha - \gamma$, respectively, do not attract much attention. The correlation between $\cos\beta$ and γ provides a peak at $\cos\beta = 0$ for negative γ, while it almost disappears at $\cos\beta = 0$ for positive γ.
These distributions enter the decomposition into the Wigner D-Functions.

6.3.4 Unnormalized Moments

Unnormalized moments can give a general survey of the contributing spins to the parent state of a decay into three pseudo-scalars, that means pions or kaons, (see section 4.2) and therefore help to identify the parent state's nature. They weight the mass spectrum of the parent system by the frequency of occurrence of given possible combinations of angular momenta and intrinsic parities. The unnormalized moments are defined by (4.37), summing up the complex values of the Wigner D-Functions $D^L_{MN}(\alpha, \beta, \gamma)$ in mass bins of the parent system for the occurring Euler Angles of the single events and a given set of LMN.
Which spins J, J' and parities η, η' can contribute to an unnormalized moment $h(LMN)$ is given by

$$|J - J'| \leq L \leq J + J' \tag{6.8}$$

$$M = m' - m \tag{6.9}$$

$$N = \mu' - \mu \tag{6.10}$$

$$\eta = (-)^{\mu+1} \tag{6.11}$$

with m, m' the projection of J and J', respectively, to the space-fixed z-axis, μ, μ' the rotationally invariant z-component of the body-fixed axis and η the intrinsic parity of the parent state. So each moment describes one or several different combinations of two sets of quantum numbers which interfere with each other.
If intermediate states are unpolarized, the decays are distributed isotropically in

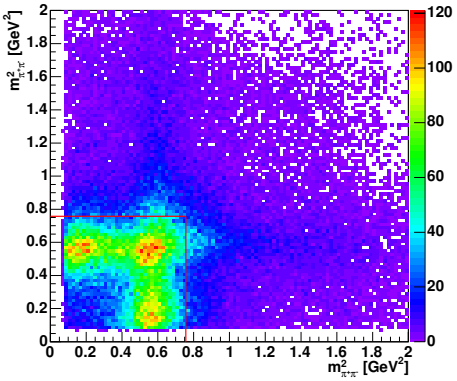

Figure 6.10: Event selection for unnormalized moments

J^P	Mesons
0^-	$\pi(1300)$
1^+	$h_1(1170)$, $a_1(1260)$
1^-	$\omega(1420)$, $\omega(1650)$
2^+	$a_2(1320)$
2^-	$\pi_2(1670)$

Table 6.1: Light mesons with potential decay $X^- \to \pi^+\pi^-\pi^-$ (from [PDG04])

space, so that the D-Function values summed up compensate each other, which means that all unnormalized moments are compatible with zero.
If an intermediate state carries spin, this results in a preferred decay direction in space, so that its interference either with itself or with another intermediate state leads to an addition of appropriate D-Functions which do not cancel out in the corresponding mass region. So the unnormalized moments which can be produced by this interference are significantly different from zero.
This method of investigating spins is sensitive to acceptance effects. For a good interpretation of data, the acceptance losses of the spectrometer have to be very small. If this is not the case, one has to correct for the acceptance effects, which is done via Monte Carlo simulations. In the analysis presented in this thesis, no Monte Carlo was performed due to time constraints, so that no acceptance corrections can be applied.
The 10 most significant real and imaginary parts, respectively, of unnormalized moments of the data sample of this analysis are shown in the following. For the presentation only events within the low mass region of the Dalitz plot ($m^2_{\pi^+\pi^-} \leq (0.87\,\mathrm{GeV})^2$, that is the region marked by the red line in figure 6.10) are selected. This region contains the ρ-bands and the $\rho - \rho$ overlap region, which is the bigger part of statistics (59 148 events), and where lots of interesting effects are expected. The high mass region is neglected, as otherwise further mass dependence would have to be taken care of [Chu05].

- The by far most significant part of an unnormalized moment is the real part of $h(202)$ (figure 6.11), which can be traced back to the potential interferences $(J^P J'^{P'})$ (1^+1^+), (2^+1^+) and (2^+2^+) at $m_{X^-} = 1.15\,\mathrm{GeV}$. Known particles with these quantum numbers in the investigated mass range can be found in table 6.1.

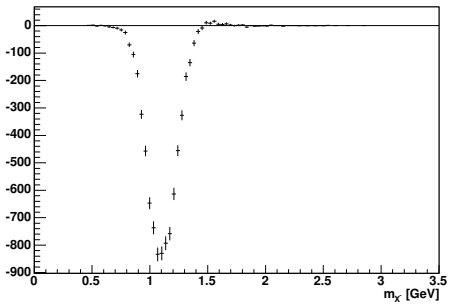

Figure 6.11: Real part of $h(202)$

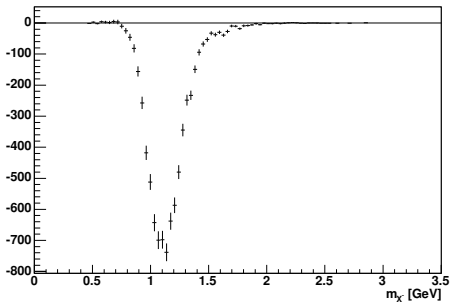

Figure 6.12: Real part of $h(200)$

- It follows the real part of the unnormalized moment $h(200)$ (figure 6.12) which is considered to be $(1^{\pm}1^{\pm})$, $(2^{+}1^{+})$ or $(2^{+}2^{+})$.
- The imaginary part of $h(101)$ (figure 6.13) can stem from $(1^{+}0^{-})$, $(1^{-}1^{+})$ or $(2^{+}1^{-})$.
- The real part of $h(210)$ (figure 6.14) can result from $(1^{\pm}1^{\pm})$, $(2^{+}1^{+})$ or $(2^{+}2^{+})$.
- The imaginary part of $h(303)$ (figure 6.15) can theoretically only be construed as $(2^{-}1^{+})$ or $(2^{\pm}2^{\mp})$, what is both unexpected, as no 2^{-} particle is known in this mass region ($m_{X^-} \approx 1.1\,\text{GeV}$). The only spin2-particle, $a_2(1320)$, has positive parity. The significance of this moment is probably created by acceptance effects of the spectrometer, but this has to be investigated with simulations.
  Mathematically interferences with one or two particles with $J \geq 3$ are imaginable as well, but it is well known that spin $J = 3$ involves a mass $m_{X^-} \geq 1.5\,\text{GeV}$, which is not provided here and can therefore be neglected.
- The imaginary part of $h(301)$ (figure 6.16), can be traced back to $(2^{+}1^{-})$.
- The real part of $h(400)$ (figure 6.17) describes the interference $(2^{+}2^{+})$.
- The real part of $h(402)$ (figure 6.18) can be produced by to $(2^{+}2^{+})$.
- The real part of $h(212)$ (figure 6.19) can be traced back to $(1^{+}1^{+})$, $(2^{+}1^{+})$ or $(2^{+}2^{+})$.
- The imaginary part of $h(111)$ (figure 6.20) can stem from $(1^{+}0^{-})$ or $(1^{+}1^{-})$.

Recapitulating, one can see that most of the significant unnormalized moments can be traced back to intermediate states which would be expected from what can be found in [PDG04], most notably $a_1(1260)$ and $a_2(1320)$ appear. Parity

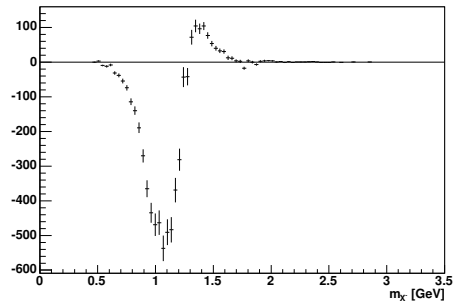

Figure 6.13: Imaginary part of $h(101)$

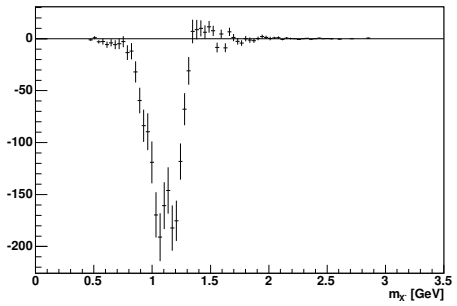

Figure 6.14: Real part of $h(210)$

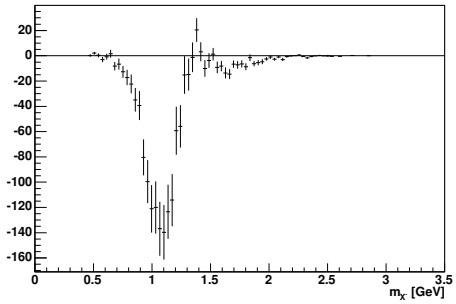

Figure 6.15: Imaginary part of $h(303)$

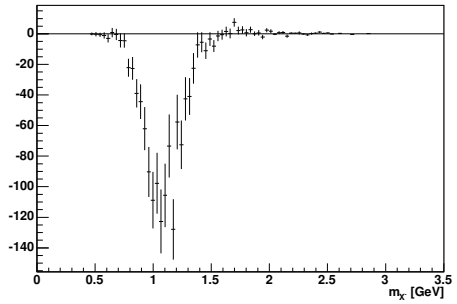

Figure 6.16: Imaginary part of $h(301)$

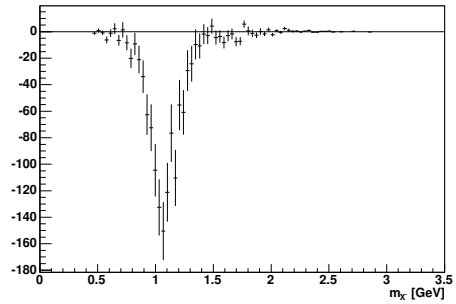

Figure 6.17: Real part of $h(400)$

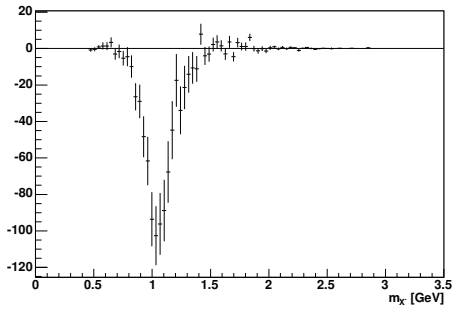

Figure 6.18: Real part of $h(402)$

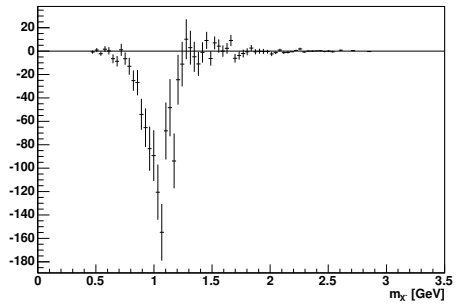

Figure 6.19: Real part of $h(212)$

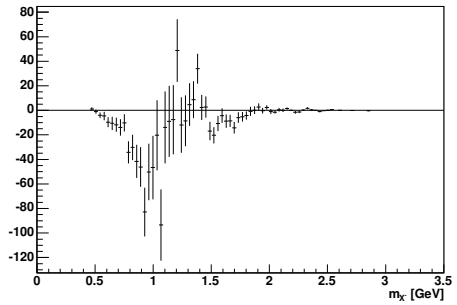

Figure 6.20: Imaginary part of $h(111)$

conservation is also seen in the data sample: For significant moments with even L, the real part is always significant, while the imaginary part is not, for odd L this is converse.
The occurrence of $J^P = 2^-$ in mass regions $m_{X^-} < 1.5\,\mathrm{GeV}$ is not clarified up to now, but is supposed to disappear after acceptance corrections have been done.

Chapter 7

Data Statistics and Quality Check

7.1 General Information

During the first hadron beam time of the COMPASS experiment, data has been taken with several different combinations of targets, beam and triggers. An overview over the recorded data is given in this section, summarized in table 7.1 in chronological order.
The 2004 beam time was mainly dedicated to the Primakoff program, with the recording of data of diffractive dissociation running in parallel. So particularly data with lead targets of 3 mm and 1.6 mm thickness were taken, also a split target with a combination of a 1 mm and a 2 mm thick lead disk was used. This data was complemented by data with 3.5 mm copper and 23.5 mm carbon targets for checking the cross section scaling with Z^2 (Z the atomic number) and data without any target ("empty target") to study the influence of the spectrometer itself.
A π^- beam with a momentum of 190 GeV, with a share of about 4.5% K^-, was used for the main part of the beam time. For comparison issues also some runs with 190 GeV muon beam were taken, to study the signature of pure electromagnetic interaction in the hadron setup, what is necessary to be well-known when performing Monte Carlo simulations for Primakoff reactions.
In the beginning of the beam time, that means up to run 42513[1], the Charge Exchange trigger was not yet included. The diffractive trigger was also switched on only in the course of the beamtime, that is from run 42820 on. For this overview, the "standard" trigger (without any notations in the relevant table element) consists of both Primakoff triggers, the calorimeter trigger (CT), the pre-scaled beam

[1]The COMPASS runs are consecutively numbered since the beginning of the experiment. In doing so, also runs for detector tests, alignment etc, are counted, as well as runs which are "bad" due to some reason or not even recorded to tape. The hadron physics data taking started with run number 42324 and ended with run number 43323.

Type of run	Trigger	Good runs			Problematic runs		
		200 spills	(<200 spills)	equiv. 200 spills	200 spills	(<200 spills)	equiv. 200 spills
π^- on empty target	- Ch_exch	2	(1)				
π^- on 3 mm Pb	- Ch_exch	15	(18)	6	7	(29)	9.5
π^- on 3 mm Pb	Prim		(1)		1	(2)	
π^- on 3 mm Pb		30	(14)	8	26	(39)	15.5
π^- on empty target		1				(1)	
π^- on 1.6 mm Pb		21	(22)	9	5	(12)	3
π^- on 1.6 mm Pb	+ Diff	9	(4)	2		(5)	2
π^- on empty target	+ Diff	4	(5)	2			
π^- on Cu	+ Diff	7	(10)	5	1	(5)	1.5
π^- on C	+ Diff	14	(8)	3.5			
μ^- on Pb	+ Diff	17	(3)	1.5	1	(1)	
μ^- on empty target	+ Diff		(4)	1			
π^- on 1+2 mm Pb	+ Diff	29	(27)	12	2	(9)	1
In total	all	155		50	43		32.5

Table 7.1: Data taken during the first hadron beam time (see text for explanations)

trigger (BT), the Charge-Exchange trigger, and the random (and lowrandom, for runs with muon beam, respectively) trigger. The runs where the Charge Exchange trigger was not yet included are marked with "- Ch_exch" in the table. The statistics taken with *Diff_1* are marked with "+ Diff". Additionally there were 4 runs taken with only the *Prim_1* and *Prim_2* triggers switched on ("Prim").
It is not trivial to determine the quality of the recorded data, as lots of things can happen during data-taking, for example problems with a detector or with a DAQ[2] computer, which can have diverse effects. For this reason the COMPASS Run Logbook [Log] contains flags for "quality" and "detectors" which are set for each run by the shift crew responsible for data taking. So this estimation is rather subjective, but a first starting point for doing quality checks. To get more reliable evaluations, it is necessary to have a detailed look at each run, what can not be performed here. The figures in table 7.1 are based on the flags from the Run Logbook: A run is considered to be good, if the quality flag is set "Good" in the Run Logbook. If the flag is set to "Prob." or is not set at all, a run is considered to be potentially problematic. The detector flag was not used to assemble this overview, but it is unexpected that a run with a severe detector problem is marked "Good". Only runs which were dedicated to physics data taking were included in the table. Runs for detector tests and the like are neglected.
The amount of data belonging to one run is defined by the number of spills it contains. The standard size consists of 200 spills. The corresponding number of runs containing 200 spills can be found in the first column belonging to good and potential problematic runs, respectively, in table 7.1. If a run is shorter, this was arranged by the shift crew. These runs can have one up to 199 spills, their numbers are each given in the second column in brackets. To get comparable quantities of shorter runs, their spills are counted and approximated how many standard runs they are equivalent to. The resulting quantities out of it can each be found in the third column.
One can estimate that the following amount of "good" data was taken:

- 141 runs with π^- on lead target of any type, therefrom 58 runs with diffractive trigger
- 12 runs with π^- on copper target, with diffractive trigger
- 17.5 runs with π^- on carbon target, with diffractive trigger
- 9 runs with π^- on empty target, therefrom 6 with diffractive trigger
- 18.5 runs with μ^- on lead target, with diffractive trigger
- 1 run with μ^- on empty target, with diffractive trigger

[2] **D**ata **A**c**Q**uisiton

7.2 Characteristics of the Analyzed Statistics

The analysis performed in chapter 6 is based on mDST files of the following data:

Run Number	42661	43228	43231
Target	3 mm Pb	1+2 mm Pb	
Trigger	Prim_1, Prim_2, CT, BT, Ch_exch, random	Prim_1, Prim_2, Diff_1, CT, BT, Ch_exch, random	
Recorded chunks (spills)	182 (110)	338 (200)	377 (200)
Analyzed Chunks	149	331	375
Total number of events	7 124 201	15 932 696	14 414 226
Number of three-particle events	177 818	615 503	579 299

Table 7.2: Statistic involved in data analysis

In total 855 chunks containing 37 471 123 events, 1 372 620 of them having vertices with three outgoing charged particles, enter the analysis.
Obviously the fraction of reconstructed three-particle events in the recorded data is about a factor 1.6 larger in the data taken with diffractive trigger compared to data taken without diffractive trigger, while the other relevant parameters, particularly the amount of target material, are equivalent. The higher fraction of three-particle events is expected, as the main character of the diffractive trigger is the requirement of two or more charged particles detected in the Multiplicity Counter (cf. section 2.2.4), while this trigger does not restrict the energies of the particles.
Based on the runs 43228 and 43231 with the diffractive trigger switched on, some further comparisons of the influence of the Primakoff triggers and the diffractive trigger on the physics results were performed. These runs contain 1 194 732 three-particle events in total. 782 967 of them feature characteristics that caused a *Diff_1* trigger signal, 572 945 of the total number satisfy Primakoff characteristics.
Figure 7.1 presents the comparison of vertices in the region between the first silicon station *SI01* at $z \approx -550\,\text{cm}$ and the *SM1*. Clear peaks can be seen at the location of the four other silicon stations ($z \approx -425\,\text{cm}, -200\,\text{cm}, -150\,\text{cm}, -100\,\text{cm}$), of the lead target at $z \approx -310\,\text{cm}$, of the scintillator at $z \approx -240\,\text{cm}$, of the scintillating fiber station *FI03* at $z \approx 124\,\text{cm}$, and the MicroMeGa stations at $z \approx 140\,\text{cm}$ and $z \approx 150\,\text{cm}$. The left figure presents the vertices of all three-particle events

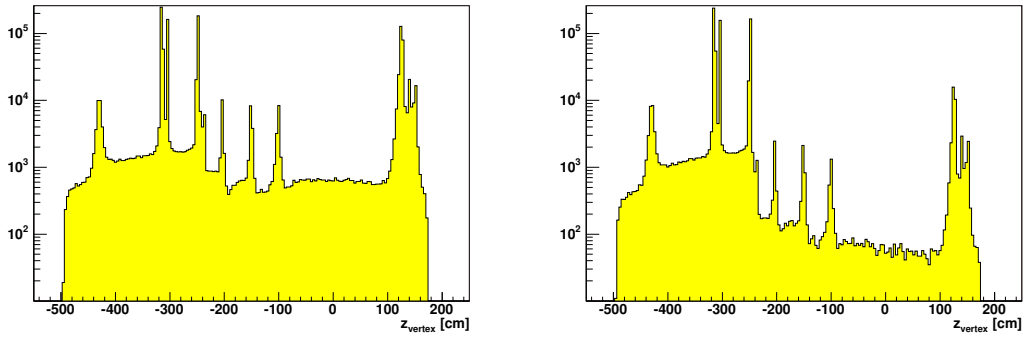

Figure 7.1: Vertex distributions for different triggers: The distribution of all three-particle events is shown in the left figure. The distribution of only events marked with diffractive trigger is presented in the right figure.

of these two runs. The right figure shows only the events that featured characteristics of the diffractive trigger. One can see that the number of events in the region up to the scintillator is in the same order of magnitude, but the number of events in the region more downstream is reduced approximately by a factor of 10. This means that the events which were not marked with the diffractive trigger have mainly vertices in the region downstream of the target and so do not enter the physics analysis due to the cut on the vertex in the lead target. If the cuts in E_X, t and z_{vertex} (see section 6.2) are applied on the data, far more than 99% of the remaining candidates feature the diffractive trigger. Thus an additional cut on the diffractive trigger seems not to be demanded. The other way round, this indicates that the data of runs taken with the diffractive trigger switched off can also be included in the analysis of diffractive interaction, as the events remaining after the cuts show the signature of diffractive dissociation as well. So this data can be used to increase the statistics, for the total beam time by an estimated factor of 1.5.

Possible acceptance effects of the other triggers than the diffractive one have not been studied so far. This has to be done thoroughly, as acceptance effects have significant influence on the angular distributions, and resulting from this on the occurring quantum numbers of the intermediate state of the investigated decay. For the analysis presented within this thesis, the influence of the acceptance effects caused by the triggers is assumed to be negligible, as only 13% of the three-particle events were not taken explicitly with diffractive trigger. Not including them into the source data for presenting the unnormalized moments, no qualitative differences appeared.

Chapter 8

Silicon Microstrip Detectors in COMPASS

Silicon microstrip detectors provide an excellent spatial resolution what makes them optimally appropriate for particle tracking in the target region of a high energy physics experiment. In the COMPASS experiment they are used for beam definition as well as tracking right behind the target in the hadron program.
A short overview of the basic operation principles of a silicon detector, based on [Bec04, Wie04], is given in section 8.1. The design of the detector modules used in the COMPASS experiment and their components is explained in section 8.2. Section 8.3 gives a description of the mounting procedure of new detector modules and the current status of the improvement of this procedure.

8.1 Basic Operation Principles

8.1.1 Elementary Silicon Properties

Intrinsic silicon is a semiconductor with an energy gap $E_g = 1.1\,\text{eV}$ between the valence band and the conduction band. If energy is deposited in the crystal, electrons can be lifted from the valence to the conduction band, leaving behind missing electrons, the so-called holes. As silicon has an indirect band gap, additional phonon excitations are needed for this process, so that at least 3.6 eV have to be deposited to create an electron-hole pair. The current in a semiconductor is given by the movement of both electrons in the conduction band and holes in the valence band.
At finite temperatures, the thermal energy ($k_B T \approx 25\,\text{meV}$, with k_B the Boltzmann constant and T the temperature) already contributes to the production of

electron-hole pairs. The intrinsic charge carrier density n_i is given by

$$n_i = AT^{3/2} \exp\left(\frac{-E_g}{2k_B T}\right) \tag{8.1}$$

with A a temperature independent constant.
The drift velocity v of electrons or holes in an external electric field E is given by

$$v = \mu E \tag{8.2}$$

with the mobility μ. The mobility depends on the temperature and the material ($\mu \sim T^{-m}$ between 100 and 400 K, with $m = 2.5$ for electrons and $m = 2.7$ for holes in silicon). Therefrom result for electrons $\mu_e = 1350\ \mathrm{cm}^2/\mathrm{Vs}$ and for holes $\mu_h = 480\,\mathrm{cm}^2/\mathrm{Vs}$ at 300 K in silicon.
The conductivity σ and the resistivity $\rho = 1/\sigma$ of a material are given by

$$\sigma = e n_i (\mu_e + \mu_h) \tag{8.3}$$

with e the elementary charge.

8.1.2 Doped silicon

The properties of a semiconductor can be modified by integrating impurities. Pentavalent atoms with one excess electron create energy levels filled with electrons close to the conduction band, so that these donor electrons can easily be excited to the conduction band (*n-type* semiconductor). Trivalent atoms with one less valence electron (acceptors) result in energy levels close to the valence band, in which the electrons from the valence band can be lifted (*p-type* semiconductor). In a doped semiconductor the current is mainly formed by the majority charge carriers, which are electrons in n-type and holes in p-type materials. The resistivity of the material thus depends on the density of the majority charge carriers: For n-type $\rho_n = 1/eN_D\mu_e$ with N_D the density of electrons, for p-type analogically.

8.1.3 pn-Junctions

A pn-junction can be produced by implanting acceptors and donors into adjoining areas of the same piece of material. The majority charge carriers start to drift to the region where their concentration is lower and they are attracted to. This region becomes charged by them, until the created electrical field prevents more charge carriers from drifting. An equilibrium results, with a region almost without any free charge carriers, called depletion zone. Any charge created in it can

be collected by electrodes, so the depletion zone is the sensitive volume for radiation detection.
To enlarge the depletion zone and the charge collection, silicon detectors are operated with reverse bias, that means an external bias voltage is applied so that electrons are attracted to the n-side and holes to the p-side. If the p-side is highly doped and the n-side only moderately (p^+n-junction), the active volume is built of the n-side of typically several 100 μm thickness, and the p-side with few μm thickness is just used to deplete it. As the mobility of electrons is higher, this combination is convenient for particle detectors. The width of the depletion zone can then be calculated as

$$D \approx \sqrt{\frac{2\epsilon V_B}{eN_D}} \tag{8.4}$$

with $\epsilon = \epsilon_r \epsilon_0$ the dielectric constant and V_B the external bias voltage. V_B has typical values of 50-100 V and it limited by the resistivity of the material.
Due to thermal excitation of electron-hole pairs, a small leakage current appears even in reverse bias. It increases with $\sqrt{V_B}$ and saturates when the detector is fully depleted.

8.1.4 Particle Detection

The mean rate of energy loss of charged particles in matter can be described by the Bethe-Bloch formula. It is based on the statistical process of many interactions with only small energy transfer.
For thin material rare interactions with large energy losses are more important. The distribution relocates towards higher values, which is given by a Landau distribution:

$$P(\lambda) = \frac{1}{\sqrt{2\pi}} \exp\left(-\frac{1}{2}(\lambda + e^{-\lambda})\right), \qquad \lambda = \frac{\Delta E - \Delta E_{mp}}{\xi} \tag{8.5}$$

with the most probable energy loss E_{mp} and a material constant ξ.
Silicon wafers are very suitable for particle detection, as the energy needed for charge carrier production (3.6 eV per electron-hole pair) is very small compared to gas detectors or photo cathodes. So the signal of a certain deposited energy is quite sharp, and the efficiency to detect passing particles is practically 100%.
Charge collection efficiency is the ratio of collected charge and charge originally deposited in the silicon. It saturates in fully depleted detectors and is also influenced by radiation damages (section 8.1.5).
The excellent spatial resolution of silicon detectors is often reached by very small

structures. Strip sizes down to 10 μm can be manufactured. The spatial resolution is connected to the pitch δx of the readout strips. If the charge cloud is completely collected on one strip, the spatial information is simply the position of the strip center, with an uncertainty $\sigma_x = \delta x/\sqrt{12}$. If the charge cloud is shared between two or more strips, the center of the cloud can be calculated with a much higher precision. For this purpose intermediate strips can be added, which are not read out, but transfer charge via capacitive coupling to increase the spatial resolution significantly.

8.1.5 Radiation Damage and Lazarus Effect

Heavy irradiation of silicon detectors, as occurs especially in high-flux hadron beams of high energy physics experiments, causes damage by incident or scattered particles colliding with lattice atoms of the silicon crystal. This leads to an increase of noise as well as to a decrease of the signal, until finally the detectors are no longer usable.
The lifetime of silicon detectors is aimed to be prolonged by manufactural optimizations or recovering the charge collection efficiency by operating the detectors at low temperatures ($\approx$ 100 K). This "Lazarus effect" is to be applied with the COMPASS silicon detectors what means several technical tasks for cooling the detectors with liquid nitrogen (see [dMa04, Bec04]).

8.2 Components and Design of the Detector Modules

Each *silicon detector station* in COMPASS consists of a custom-built *cryostat* appropriate for cryogenic operation, where two silicon detector *modules* are assembled and also the infrastructure for cooling, cryogenics, electronics and vacuum is integrated, and furthermore readout electronics and cooling accessories outside the cryostat (for the setup see [Fuc03, dMa04]). In this section the configuration of the detector modules, consisting of the silicon wafer sandwiched between two frontend boards carrying readout electronics and cooling facilities, is briefly described (for more details see [Wie04, dMa04, Bec04]).

8.2.1 Silicon Wafer Design

COMPASS uses double-sided silicon microstrip wafers which were originally designed for the HERA-B experiment. The wafers were developed by the Halbleiterlabor of the Max-Planck-Institut für Physik in Munich, where great importance

was attached to radiation hardness. A multi guard-ring structure makes the application of higher bias voltages (up to 500 V) possible, which are needed for full depletion after radiation damages. For capacitive coupling of the readout electronics to the detector, thin separation layers of silicon dioxide and silicon nitride are implemented. Additionally, polysilicon resistors of $\sim 1\,\mathrm{M}\Omega$ are used for strip biasing instead of punch-through contacts.
The silicon wafer consists of a 280 μm thick n-type silicon substrate with $2-3\,\mathrm{k}\Omega$ resistivity. Its active area covers 50 mm $\times$ 70 mm. The n-side contains 1280 readout strips with a pitch of 54.67 μm, while the p-side provides 1024 readout strips with a pitch of 51.75 μm and additional 1023 intermediate strips to improve the spatial resolution.
The strips on the n-side are perpendicular to the ones on the p-side, each tilted by an angle of 2.5° with respect to the edge of the wafer. So if two detectors are mounted back-to-back a stereo angle of 5° is achieved. This leads to four projections for each particle passing, allows tracking, and makes it possible to disentangle multi-hit ambiguities.

8.2.2 Frontend Electronics

The COMPASS silicon detectors are operated with a bias voltage of approximately 100 V. The signal induced in the silicon strips by a crossing particle has to be collected, amplified and digitized, before it can be sent via the readout chain to the COMPASS data acquisition. The beginning of this procedure is performed by the readout chip APV25[1] S1. This chip was developed for the silicon trackers of the CMS experiment at CERN and fits the demands of the COMPASS silicon detectors.
The APV25 chip is a 128 channel analog pipeline ASIC[2]. The signals of each channel are preamplified and reshaped into a well defined voltage pulse with a peaking time of 50 ns. The amplitudes are sampled continuously every 25 ns and stored in an analog pipeline with 160 buffer cells made of capacitors. This compensates the trigger latency: If a trigger request arrives, the buffer cells with the respective latency are read out and the signals are formed to differential currents by an output multiplexer.
The APV25 chips are used in the so-called *multi-mode*. So three consecutive pipeline columns are read out, from which the pulse shape can be reconstructed in order to improve the time resolution.

[1] **A**nalog **p**ipeline **v**oltage-type
[2] **A**pplication **S**pecific **I**ntegrated **C**ircuit

8.2.3 The Frontend Boards "L-board"

The support structure of a silicon detector module consists of a set of two L-shaped 6-layer PCBs[3] of 1 mm thickness. These boards fix the silicon wafer and host the APV25 chips and the infrastructure for them as well as for the cooling facilities.
One L-board hosts 10 chips to read out the 1280 channels of the long n-side of the wafer (called L10), while the other one (L8) hosts 8 chips connected to the 1024 strips of the short p-side.
The L-boards also provide cooling rails with copper layers and metalized holes in the PCB as well as pads where two PT100 temperature sensors can be attached. Space for connectors for power lines and signal lines is furnished on the boards, too.

8.2.4 Cooling facilities

To cool the silicon wafers with liquid nitrogen, thin Cu/Ni capillaries (with diameters of $d_{outer} = 1.6\,\text{mm}$ and $d_{inner} = 1.3\,\text{mm}$) are soldered to the backside of the inner margin of the L-boards. These capillaries can also be flushed with gaseous nitrogen for a moderate cooling during the warm operation of the detector. Simulations showed that it is sufficient to cool the wafer on two sides. So the capillaries are soldered only on the two readout sides, to thermally separate the cooled silicon from the heat producing readout chips.
As the two L-boards are on different electrical potential due to the bias voltage applied at the silicon wafer, the two capillaries have to be electrically separated. To have only one cooling loop per module, the capillaries are connected via a custom-made electrical insulating connector cast made of epoxy glue[4].

8.2.5 Configuration of the Detector Modules

A picture of a complete silicon detector module is presented in figure 8.1. The schematic cross-section of a L-board can be seen in figure 8.2.
The silicon wafer is sandwiched between the two L-boards. First the L10 with chips up is placed, then follows the wafer with n-side up (and bond pads next to the chips of L10). The third layer is the L8 with chips below, next to the bond

[3] **P**rinted **C**ircuit **B**oard

[4] The two component epoxy glue "Uhu endhart 300" is used to cast this connector with a custom mold made of teflon. The tubular form for the nitrogen flux is kept free with a teflon wire during the casting process.

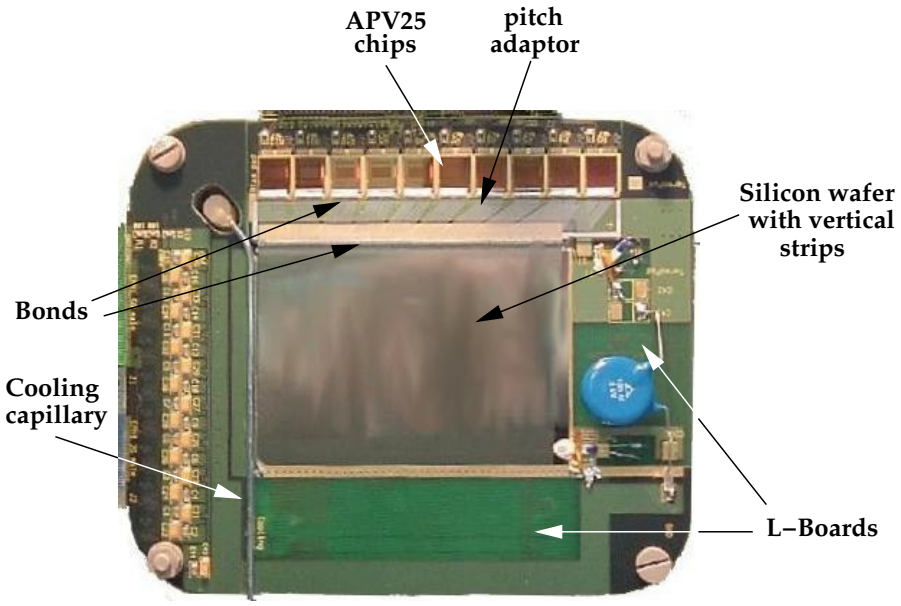

Figure 8.1: A complete silicon detector module [Bec04]

pads of the p-side of the wafer. The wafer is glued to the L-boards on the 1.5 mm small margin of the inner border of the boards. A special silicone glue with very small electrical conductance and good flexibility at low temperature is used for this.
The APV25 chips are glued to the boards with Epoxy E-Solder, a two component conductive glue. To avoid noise on the power and grounding lines of the chips, capacitors (100 nF tantal, 10 μF electrolyte) are mounted between the power lines on the backside of the boards, two capacitors of each kind to one chip.
To match the silicon bonding pads and the APV25 input pads, a pitch adapter is glued on the chip-side of each L-board, which is bonded to the respective pads. As it provides structures down to 9 μm, it cannot be made of PCB and is manufactured with aluminum wires on 300 μm thick glass.

8.3 Enhancement of the Production Procedure of new Detector Modules

During the first hadron beam time 2004, five silicon stations were operated, two before and three directly after the target. For the muon beam time in 2006, it is foreseen to have three silicon stations as beam trackers. For the beam time 2007 hadron beam is on the agenda. Therefore it is planned to have five cryogenic silicon stations, therefrom four stations are to be built completely new. This means,

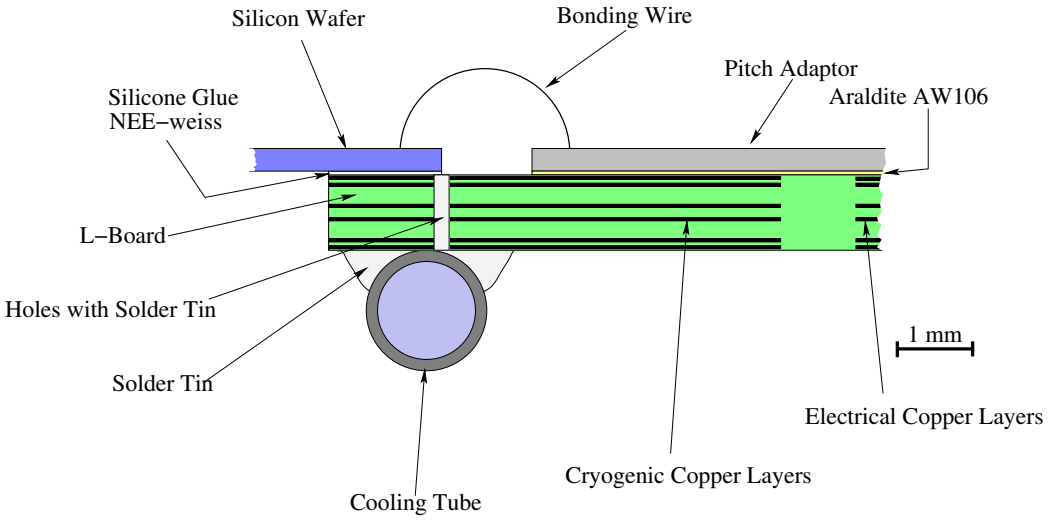

Figure 8.2: Cross-section of a L-board (from [Wie04])

that apart from all the other necessary infrastructure, eight new detector modules have to be produced.
Several preparations for mounting new detector modules have been performed within this thesis. A list containing all necessary components for one module can be found in appendix A. The infrastructure and knowledge to mount detector modules had to be recovered and were tried to optimize.
The previous mounting procedure for modules of the COMPASS silicon detector is described in appendix B. The instruction given there is based on the instruction given to an external company in 2004, complemented by some additional explanations, based on realizations during understanding the procedure and on [Wie05].
Some potentially problematic points of this procedure have been found and the following improvements are planned or under investigation:

- For gluing the APV25 chips to their pads on the L-boards a two component conductive glue is used, the Epoxy E-Solder 3025. This glue is chosen as electrical conductivity between a chip and its ground pad on the L-board is necessary for operating the APV25 chips, but the glue is very tough and not very comfortable to handle. Additionally the glue is not intended to be used with cryogenic temperatures, breaking of the splices is risked and is observed in some used detector modules. A similar two component conductive glue produced by the same American company, Epoxy E-Solder 3083, which is designed for larger temperature regions and could be more appropriate also for cryogenic temperatures, exists but is not available in

Europe. Another potential improvement could be gluing with a conductive foil which is used to stick the APV25 chips of the COMPASS GEM detectors [Ket05], but its behavior at cryogenic temperatures has to be tested thoroughly.

- The splices of the silicon wafer to the L-boards have also to be improved. With all previous detector modules the silicon wafers were glued to the L-boards on all four sides. It turned out that with frequent rapid changes between cryogenic and room temperature the wafer runs the risk to break near the warmest edge of the L-board, where the mechanical stress due to the temperature difference is greatest. During tests of the cryogenic setup, three modules with broken wafers were observed [Bec04]. This is confirmed by simulations [Fri05] which also show that this problem can be solved with gluing the silicon only on the two sides where the L-board is cooled as well. The remaining silicone glue is still enough to fix the wafer, which is shown by some modules which were operated for several cycles at cryogenic temperatures, and where the silicone glue came off due to the mechanical stress mentioned above. For these reasons it was decided to glue the wafers of future modules only on two sides.

- The first gluing step of the wafer to the L-boards is the sticking of the wafer to the L10. The L10 is mounted on a jig #2 (see appendix B.3) and clamped onto the *xyz*-table, lower than the adjustable vacuum table which is situated in its center. The wafer on the vacuum table is iteratively lowered until the vacuum drops, this can lead to severe mechanical stress for the wafer if not arranged with enough caution. Additionally some weight is put on the silicon during the drying process which is also precarious. An improvement could be to rearrange this setup: One can construct a jig where the L-board is attached in a way that the wafer on the vacuum table is pressed against it. This means that instead of lowering the wafer with the vacuum table and gluing it on top of the L-board, it is suggested to lift the wafer and glue it onto the bottom of the L-board. To align the wafer on the L-board properly this jig would have to have holes in the region of the edges of the wafer.

- The next gluing step of the L8 onto the L10 with the wafer is similarly susceptible as the first one. The L8 and the L10 with the wafer are each clamped in a respective jig #2, the jig with the L10 still mounted on the *xyz*-table. The L8 is put on top of it and is lowered until the correct distance between the wafer and the L8 of $\sim 50\,\mu$m is reached. In this position the distance spacers are fixed. Afterwards both jigs are raised and turned around, so that the L10 can be glued on top of the L8. This handling of L-boards clamped in jigs is ticklish and to be minimized due to the sensibility of the parts of the mod-

ule. This could be achieved by designing a new jig which redundantizes turning around during the mounting.

- For the gluing of the second L-board to the first one which is already glued to the wafer, precision screws act as distance pieces and can be optimized as well. The current ones are equipped with pikes which can cave into the aluminium of the jigs in continuous use and should be replaced by precision screws with bullets which are equally accurate.

Chapter 9

Conclusion and Outlook

An elementary analysis of the diffractive dissociation of 190 GeV π^- beam on lead into three charged pions is presented in this thesis. An overview of the principles of diffractive interaction is given as well as an introduction to the unnormalized moments. Those are very adjuvant to get an impression of the spins of the intermediate states.
The analysis is based on data of the first COMPASS hadron beam time in 2004. The selection of events featuring diffractive characteristics is based on the exclusivity peak of the energy distribution of the three-particle system, small momentum transfer and a vertex in the lead target. The total mass of the three-pion system X^- provides a significant peak at $m_{X^-} = 1.15\,\text{GeV}$ with a shoulder at $m_{X^-} = 1.3\,\text{GeV}$, and a slight peak at $m_{X^-} = 1.7 - 1.8\,\text{GeV}$. The Dalitz plot shows the $\rho(770)$ excitation in the $\pi^+\pi^-$ systems clearly. The significant unnormalized moments mainly point out well-known intermediate states, particularly the $a_1(1260)$ and the $a_2(1320)$. The unexpected occurrence of states with $J^P = 2^-$ in the mass region $m_{X^-} < 1.5\,\text{GeV}$ could not be clarified, but is supposed to be an acceptance effect. Therefore in the further analysis acceptance corrections have to be done with Monte Carlo simulations of the spectrometer.
The analysis will be extended to the full statistics taken during the hadron beam time. To get more reliable results of the spins of the intermediate states, partial wave analysis will be performed on the full statistics, starting from the results from the unnormalized moments and the acceptance corrections.
For the beam time 2007, four new silicon stations are planned to be built. The knowledge and the infrastructure to mount new detector modules for them were recovered within this thesis. Improvements for the mounting procedure, concerning the gluing of the APV25 chips, the gluing of the silicon wafer, and the handling of the susceptible parts of the detector modules, were developed and are under further investigation.

Appendix A

Material needed for Mounting one Silicon Detector Module

The lists stated below include all constituents and auxiliary materials which are needed for mounting one detector module. Descriptions of the custom-built components can be found in section 8.2.

silicone glue NEE-001 weiß
Epoxy E-Solder
Uhu plus / Uhu hart / Araldit
heat conductive paste
jigs #1 (to hold tight the L-boards during their prearrangement)
jigs #2 (for support and keeping the right distance during the gluing of the wafer)
bonding frame (jig #3) or transportation frame
xyz-table
soldering accessories
dispenser with suitable dose tips
wire fitting inside the capillary
sand paper 800
kapton tape
wire with $\sim 50\,\mu$m thickness for spacer

Table A.1: Auxiliary materials

1	silicon wafer
1	L-board L10
1	L-board L8
1	pitch adapter 10-side
1	pitch adapter 8-side
18	readout chips APV25 S1
37	ceramic capacitors 100 nF 0805
37	tantal capacitors 10 μF
1	high-voltage capacitor 10 nF, 3 kV
18	resistors 4.7 kΩ 0603
4	resistors 100R 0603
1	resistor 12R 0603
1	resistor 10R 0603
1	ERNI connector 90° 26 pins
1	ERNI connector 90° 50 pins
1	ERNI connector 26 pins
1	ERNI connector 50 pins
1	epoxy connector
2	Cu/Ni capillaries (20 cm long, diameters $d_{outer} = 1.6$ mm and $d_{inner} = 1.3$ mm)
4	PT100 temperature sensors
2	spacers of 300 μm glass fiber

Table A.2: Constituents of one detector module

Appendix B

Instruction for Mounting Silicon Detector Modules

These instructions for mounting silicon detector modules, including the pictures presented, are based on the instructions worked out for an external company which mounted some modules in the beginning of 2004. The procedure is described with some illustrative additions.

B.1 Preparations

Before starting the mounting procedure, assure that the following preparations are carried out:

- Make sure that all necessary components (cf. appendix A) are available, especially that the silicone glue and the Epoxy E-Solder are still serviceable
- Make the positioning holes into the L-boards: These are precision holes which can be drilled in the precision mechanics workshop with the specific clamped support and a special program.
- Prepare the tubes
  - Use a sharp scalpel to carve outside around the capillaries several times until they can be broken easily (take care that they do not twist)
  - Put the wire inside the capillaries, then bend them so that they fit the L-boards and the epoxy connector and lie completely on the respective board; some centimeters of tube have to be reserved on both ends.

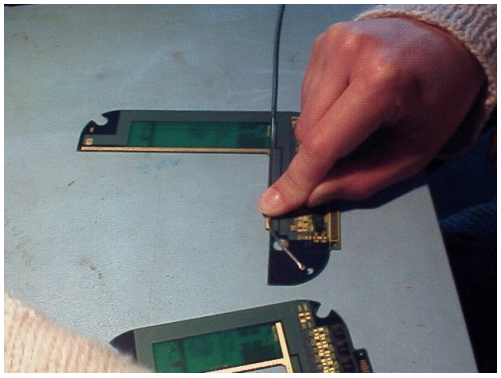

Figure B.1: Adaptation of the capillary

Figure B.2: The presolder bath

  - Clean the capillaries with sand paper 800
  - Close bended end with pliers to avoid presolder coming in
  - Apply presolder bath: Put the tubes into liquid solder tin in a hot pot, so that a thin film of solder tin is generated outside of the tube.

- Trim to fit spacers (glass fiber, 300 μm thick) for being glued between the splices of the L-boards

B.2 Prearrangement of Single L-Boards

First SMD components and the capillary are soldered to the backside of the L-boards, then SMD components, ERNI connectors, pitch adapter and APV chips are mounted to the topside.

B.2.1 Backside

- Clean the L-boards with isopropilic alcohol
- Apply kapton tape on the top side of the L-boards to avoid the soldering paste from the tube not only going through the vias[1], but also distributing on the top side
- Fix the board on a ceramic support with crocodile clamps and kapton tape to avoid bending during the soldering

[1] Vias are diminutive metalized holes through the L-board on the area of support of the capillaries. When the capillary is soldered in the oven, part of the presolder flows into them and enables thermal conductivity between the capillary and the cryogenic copper layers in the L-board (see figure 8.2, “Holes with Solder Tin”)

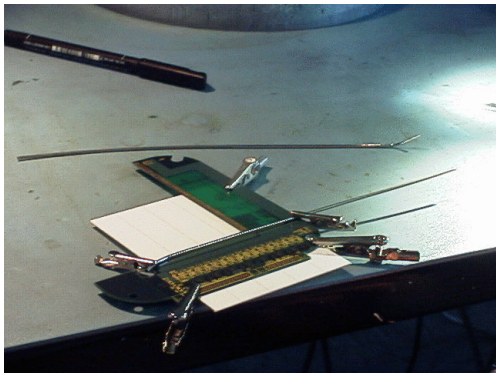

Figure B.3: Fixed tubes

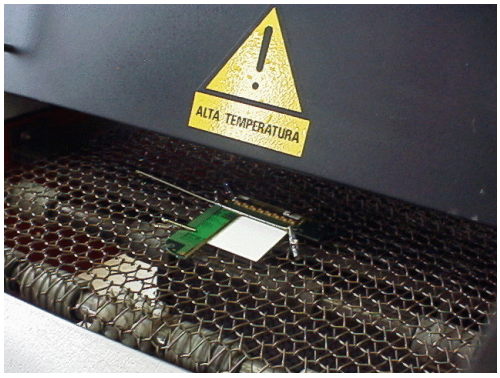

Figure B.4: The oven

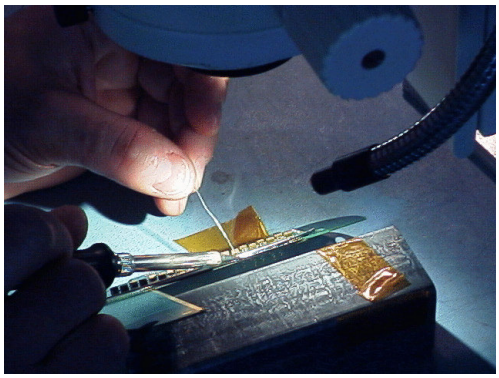

Figure B.5: Soldering of tubes

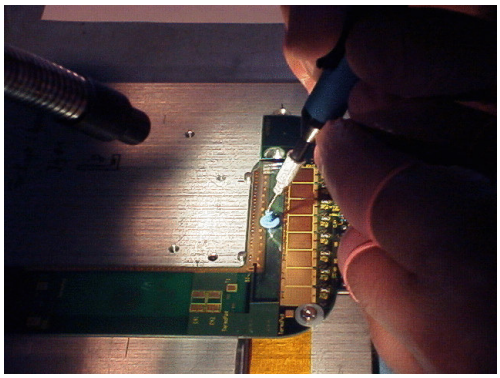

Figure B.6: Gluing the pitch adapter (1)

- Apply solder paste on the long pad
- Mount SMD components according to drawing and color code, using solder paste
- Solder backside components in infrared oven
- On L10 mount the tube by hand and solder gun

B.2.2 Topside

- Mount SMD components with solder paste and heat gun
- Mount ERNI connectors: Cut one ear (L10, 50pin, right side) and solder connectors by hand according to drawing
- Fix L-boards to jigs #1
- Glue pitch adapters

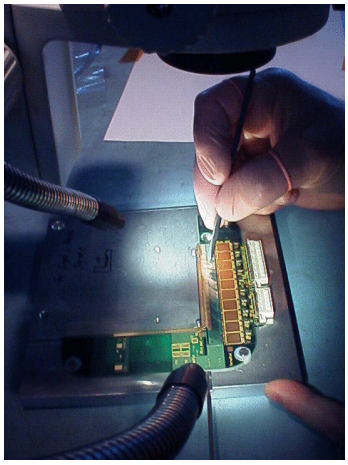

Figure B.7: Gluing the pitch adapter (2)

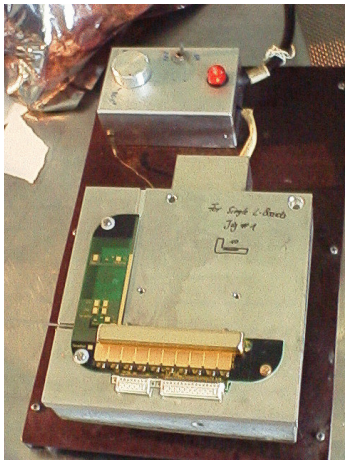

Figure B.8: Gluing the pitch adapter (3)

  - Put kapton tape on the backside of the board, to avoid that the glue flows into the vias
  - Spots of "Uhu hart" (Araldit) in two lines (with the green dispenser tips)
  - Align the pitch adapter to the two reference crosses on the PCB
  - Put weight (e.g. brass block) with some protection (thin Teflon coat) onto the pitch adapter to gain flatness required for bonding
  - Heating plate at 90°C for 30 min

- Glue readout chips APV25 S1
  - Put small spots of two component conductive glue (Epoxy E-Solder) (12-16 spots with the green tip, operate the dispenser at a pressure of 5.5 bar), so that there is enough glue to stand thermal stress at 130 K, but no shortcuts due to "squeezed glue" (especially on the front and pack pads)
  - Align the chips on the front side with the pitch adapter, center the chips on the back side between the pads on the PCB
  - Polymerize the E-Solder 4h at 40°C and leave it over night at room temperature (never oven with more than 40°C, chips can move otherwise)

B.3 Gluing of the Silicon Wafer

- Glue the glass fiber spacers onto L10, on the splices of the L10 with the L8

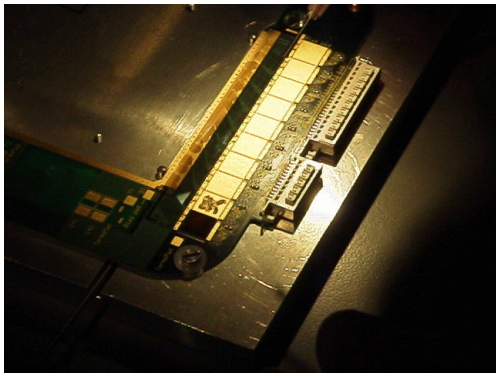

Figure B.9: Gluing the APV25 chips

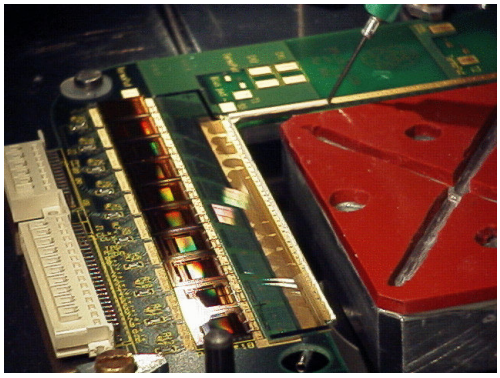

Figure B.10: Silicone glue

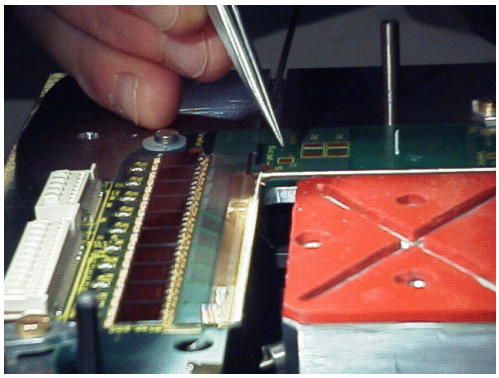

Figure B.11: The spacer wires

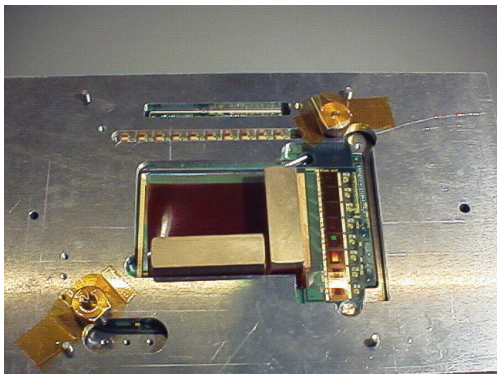

Figure B.12: Drying position

- Mount the L-boards on the jigs #2, using positioning pins, adapters, screws and kapton tape
- Glue the wafer onto the L10
  - prepare wires $\sim 50\,\mu$m, $\sim 1.5\,$cm long as spacer
  - Fix the jig with the L10 on the xyz-table with positioning pins
  - Put a continuous line of mono component silicone glue, as much as "possible": squeezing out of glue is acceptable, preferably on the inner side of the silicon; (green tip, 3 bar for fresh glue, $\sim 400 - 500\,\mu$m line thickness, a little bit inside the PCB (0.1 mm))
  - Attach spacer wires, pointing downward perpendicular to the edge of the L-board (5 wires long side, 4 wires short side)
  - Mount silicon wafer on the vacuum table
  - Align and lower the silicon iteratively to the inner side of the reference cross on the PCB; lower until the vacuum "sucks", then retreat
  - Put weight (2 brass bars $15 \times 15 \times 50\,\text{mm}^3$) on the silicon, inclusive some protection

  - Let the silicone glue dry for about 12 hours (final hardness is only reached after 2-3 days)
  - Remove the spacer wires

- Glue the L8 onto the wafer on the L10
  - Prepare 50 μm wires as spacers, $\sim$ 1.5 cm (not too long, else they will rotate during mounting)
  - Adjust screws for correct distance between jigs:
    * Put L8 on top of L10
    * Lower L8 until distance silicon - L8 is $\sim$ 50 μm in the main diagonal (maybe one can use kapton foil for this)
    * Equalize distance between the two jigs in the main diagonal, using the spacer fingers
    * Set the distance of the jigs in the side diagonal to distance measured in main diagonal
  - Apply silicone glue, analogue to L10
  - Fix wires: Chip side (short side of L8) downward, non-chip side (long side) with kapton tape to the PCB
  - Put L10 on top of L8 with the positioning pins for alignment
  - Final polymerization time $\sim$ 2-3 days

B.4 Residual Steps and Remarks

- Insert the epoxy connector, glue the tubes to the epoxy connector with Uhu glue; polymerization at room temperature for 24 hours
- Remarks:
  - Once the tube is glued, blow it out with air to check that the tube was not closed
  - Do not cut the glue and do not treat the glue with alcohol - otherwise the system will not be vacuum tight
- Stick the PT100 temperature sensors, one onto the edge of the wafer (with L10), the others onto the L-boards
- Solder the high-voltage capacitor to the respective pads on the L-boards

- Bond the detector as soon as possible, to avoid oxidizing of the bond pads. That means make micro-wire connections between the silicon wafer and the pitch adapter, the pitch adapter and the APV chips, the APV chips and the according pads on the L-boards.
- Store the completed detector modules in dry and low oxygen environment.
- See also the list of suggestions for improvements of the assembling procedure in section 8.3.

List of Figures

List of Tables

Bibliography

[AJM76] U. Amaldi, M. Jacob, and G. Matthiae. Diffraction of hadronic waves. *Ann. Rev. Nucl. Sci.* **26**, 385–456 (1976). (Cited on page 21.)

[Bec04] M. Becker. *Setup of a Cryogenic System for Silicon Microstrip Detectors in the COMPASS Experiment*. Diploma thesis, Technische Universität München, September 2004. (Cited on pages 57, 60, 63, 65, and 80.)

[Bru97] R. Brun and F. Rademakers. ROOT: An object oriented data analysis framework. *Nucl. Inst. Meth.* **A389**, 81 (1997). (Cited on page 14.)

[CER] CERN web site, `http://www.cern.ch/`. (Cited on page 3.)

[ChT75] S. U. Chung and T. L. Trueman. Positivity conditions on the spin density matrix: A simple parametrization. *Physical Review D* **11 3**, 633–646 (1975). (Cited on page 30.)

[Chu71] S. U. Chung. Spin Formalism. *CERN Yellow Report* **CERN 71-8** (1971). (Cited on pages 27, 28, and 30.)

[Chu02] S. U. Chung et al. Exotic and $q\bar{q}$ resonances in the $\pi^+\pi^-\pi^-$ system produced in $\pi^- p$ collisions at 18 GeV/c. *Physical Review D* **65 072001** (2002). (Cited on pages 34 and 79.)

[Chu05] S. U. Chung, `suchung@rcf.rhic.bnl.gov`. Private communication, 2005. (Cited on pages 22, 23, 26, 29, 47, 79, and 81.)

[COM96] The COMPASS Collaboration. A proposal for a Common Muon and Proton Apparatus for Structure and Spectroscopy. *CERN* **SPSLC 96-14** (1996). (Cited on page 3.)

[COM05a] The COMPASS Collaboration. First Measurement of the Transverse Spin Asymmetries of the Deuteron in Semi-inclusive Deep Inelastic Scattering. *Physical Review Letters* **94 202002** (2005). (Cited on page 5.)

[COM05b] The COMPASS Collaboration. Gluon polarization in the nucleon from quasi-real photoproduction of high-p_T hadron pairs. *CERN-PH-EP* **2005-049** (2005). (Cited on page 4.)

[COM05c] The COMPASS Collaboration. Measurement of the spin structure of the deuteron in the DIS region. *Physics Letters B* **612**, 154–164 (2005). (Cited on page 5.)

[COM05d] The COMPASS Collaboration. Search for the $\phi(1860)$ Pentaquark at COMPASS. *European Physics Journal C* **41**, 469–474 (2005). (Cited on page 6.)

[COM06] The COMPASS Collaboration. Setup and Performance of the COMPASS Experiment at CERN. *Publication in preparation* (2006). (Cited on page 7.)

[COR] CORAL web site, `http://coral.cern.ch/`. (Cited on page 14.)

[dHo04] N. d'Hose et al. Possible Measurements of GPDs at COMPASS. *Workshop Contribution to Future Physics @ COMPASS, CERN* (2004). (Cited on page 5.)

[dMa04] R. de Masi. *Development of a cryogenic silicon detector system and study of strange particle production in deep inelastic scattering*. PhD thesis, Technische Universität München, July 2004. (Cited on page 60.)

[Fer05] A. Ferrero. Soft hadronic interactions in the COMPASS experiment. *Czech. J. Phys.* **55** (2005). (Cited on pages 35 and 36.)

[Fri05] J. Friedrich, `friedric@ph.tum.de`. Private communication, 2005. (Cited on page 65.)

[Fuc03] A. Fuchs (married Dinkelbach). *Setup of a low Temperature Silicon Detector for the COMPASS Experiment*. Diploma thesis, Technische Universität München, December 2003. (Cited on page 60.)

[Gou83] K. Goulianos. Diffractive interaction of hadrons at high energies. *Physics Reports* **101 3**, 169–219 (1983). (Cited on page 19.)

[Gru06] B. Grube. *A Trigger Control System for COMPASS and A Measurement of the Transverse Polarization of Hyperons from Quasi-Real Photo-Production*. PhD thesis in preperation, Technische Universität München, 2006. (Cited on pages 5, 8, 15, and 79.)

[Kac02] Kachaev I. Study of reaction $\pi^- A \to \pi^+\pi^-\pi^- A$ at VES setup. In *AIP Conf. Proc. 619: Hadron Spectroscopy*, pages 577–581, June 2002. (Cited on page 33.)

[Ket05] B. Ketzer, `bernhard.ketzer@cern.ch`. Private communication, October 2005. (Cited on page 65.)

[Log] COMPASS Run Logbook, `http://wwwcompass2.cern.ch/runLogbook/dirphp/`. (Cited on page 53.)

[Nag05] T. Nagel. *Cinderella: an Online Filter for the COMPASS Experiment*. Diploma thesis, Technische Universität München, January 2005. (Cited on page 13.)

[PDG04] Particle Data Group. *Review of Particle Physics*, volume 592. 2004. (Cited on pages 22, 47, 48, and 81.)

[PHA] PHAST web site, `http://ges.home.cern.ch/ges/phast/`. (Cited on page 15.)

[ROO] R. Brun, F. Rademakers, et al. ROOT home page, `http://root.cern.ch`. (Cited on page 14.)

[Ros57] M. E. Rose. *Elementary Theory of Angular Momentum*. John Wiley & Sons, Inc., New York, 1957. (Cited on page 28.)

[Wie04] M. Wiesmann. *A Silicon Microstrip Detector for COMPASS and a First Measurement of the Transverse Polarization of the Lambda-Hyperons from Quasi-Real Photo-Production*. PhD thesis, Technische Universität München, January 2004. (Cited on pages 5, 57, 60, 64, and 80.)

[Wie05] M. Wiesmann, `wiesmann@ehfs.de`. Private communication, October 2005. (Cited on page 64.)

Own Contributions

This thesis has been done within the framework of the chair of Prof. Dr. Paul at the Technische Universität München and at the COMPASS collaboration at CERN, Geneva.
The major part of this thesis was spent on the data analysis starting with analyzing the first mDSTs from the November pre-production of 2004. Those were produced just some days before this thesis started. I developed my own PHAST `UserEvent` function for the analysis step by step under the supervision of Jan Friedrich.
Much time was spent in getting familiar with the unnormalized moments. The theory was presented by Suh-Urk Chung in the lecture "Hadron Spectroscopy" at TUM during the summer term 2005. Based on this lecture and several additional informal meetings, the calculations of the Euler Angles and furthermore of the unnormalized moments were added to the PHAST function. This function was carefully checked due to its complexity and had to be adapted several times.
I also took part in several analysis meetings of the COMPASS collaboration and presented my analysis with three talks during the course of this year.
During the last part of this thesis I prepared the production of new COMPASS silicon detector modules which has to be carried out in 2006. I arranged a complete list with all the required material and ordered all the components and auxiliaries. I also retraced the production procedure of the detector modules. During an informal meeting with Anna-Maria Dinkelbach and Michael Wiesmann problematic parts of the current procedure were discussed and several potential improvements were developed.

Acknowledgments

First I would like to thank Prof. Dr. Stephan Paul for giving me the chance to study an exciting topic of modern particle physics. Several trips to CERN gave me a deeper insight into the COMPASS physics as a part of the fascinating world of high energy physics.
Jan Friedrich deserves sincere thanks for continuous and patient supervision throughout the whole year. He was always disposed to respond even to naive questions and to explain things in a major context, thereby I could learn a lot about physics.
Many thanks go to Suh-Urk Chung, who introduced the unnormalized moments not only in the lecture, but was willing to give me repeated guidance during this part of the analysis.
I'd like to thank Anna-Maria Dinkelbach and Michael Wiesmann for discussing the hardware part of this thesis with me and impart their knowledge and experience with the COMPASS silicon detector.
I am grateful to Boris Grube, Roland Kuhn and Alexander Mann for help with computer and programming problems. Boris and Roland developed the TEXframework this thesis is based on. Alexander was always helpful with varied little problems, and he also taught me how to solder SMD components onto L-boards.
Additionally I'd like to thank Dmitri Ryabtchikov for providing the cross-check for the first part of the analysis for a potential release and giving several suggestions.
Further thanks go to Annemarie, Jan, Boris, Suh-Urk and Bernhard Ager for proof-reading the manuscript and giving several improving hints.
Größter Dank gebührt meinen Eltern, die mir das Physikstudium ermöglicht haben und mich die ganze Ausbildungszeit hindurch unterstützt und ermutigt haben, meinen eigenen Weg zu finden.